IMPACT OF A COSMIC BODY INTO EARTH'S OCEAN AND THE GENERATION OF LARGE TSUNAMI WAVES: INSIGHT FROM NUMERICAL MODELING

K. Wünnemann,[1] G. S. Collins,[2] and R. Weiss[3]

Received 4 September 2009; revised 15 July 2010; accepted 26 July 2010; published 24 December 2010.

[1] The strike of a cosmic body into a marine environment differs in several respects from impact on land. Oceans cover approximately 70% of the Earth's surface, implying not only that oceanic impact is a very likely scenario for future impacts but also that most impacts in Earth's history must have happened in marine environments. Therefore, the study of oceanic impact is imperative in two respects: (1) to quantify the hazard posed by future oceanic impacts, including the potential threat of large impact-generated tsunami-like waves, and (2) to reconstruct Earth's impact record by accounting for the large number of potentially undiscovered crater structures in the ocean crust. Reconstruction of the impact record is of crucial importance both for assessing the frequency of collision events in the past and for better predicting the probability of future impact. We summarize the advances in the study of oceanic impact over the last decades and focus in particular on how numerical models have improved our understanding of cratering in the oceanic environment and the generation of waves by impact. We focus on insight gleaned from numerical modeling studies into the deceleration of the projectile by the water, cratering of the ocean floor, the late stage modification of the crater due to gravitational collapse, and water resurge. Furthermore, we discuss the generation and propagation of large tsunami-like waves as a result of a strike of a cosmic body in marine environments.

Citation: Wünnemann, K., G. S. Collins, and R. Weiss (2010), Impact of a cosmic body into Earth's ocean and the generation of large tsunami waves: Insight from numerical modeling, *Rev. Geophys.*, *48*, RG4006, doi:10.1029/2009RG000308.

1. INTRODUCTION

[2] The collision of cosmic bodies is one of the fundamental processes in the solar system and key to understanding the origin and evolution of planets and their satellites. The heavily cratered landscapes throughout the solar system testify to the violent history of most planetary objects. In contrast, very few craters are directly visible on Earth's surface. The search for impact structures has revealed no more than approximately 170 crater structures of confirmed impact origin on Earth so far, mainly on old continental shields. However, the paucity of known terrestrial impact structures on Earth relative to the other solid surfaces in the inner solar system does not mean that Earth's past was any less violent. The limited evidence of cosmic impact in Earth's geological record instead reflects the facts that Earth's surface is continuously modified and replaced, that a thick dense atmosphere protects it, and that more than two thirds is covered by water. In particular, the latter implies that on Earth, impact in the marine environment is more common than impact on land. Hence, understanding the effect of a surface water layer on the impact process is imperative for reconstructing Earth's historical crater record and quantifying the hazard of future impact.

[3] Any assessment of the terrestrial impact hazard starts with the question of how often impacts occur on Earth. The size-frequency distribution of impacts on planetary surfaces in the inner solar system does not differ significantly, and the more complete crater records on the Moon and Mars can be used to estimate the impact frequency on Earth [*Neukum et al.*, 2001]. Crater counts on the Moon and Mars, for example, show that the number of craters above a given size decreases with crater size according (very approximately) to a power law. Thus, the number of large craters observed on extraterrestrial surfaces is much smaller than the number of small craters, and hence, the average interval between

[1]Museum für Naturkunde, Leibniz Institute at the Humboldt-Universität zu Berlin, Berlin, Germany.
[2]Impacts and Astromaterials Research Centre, Department of Earth Science and Engineering, Imperial College London, London, UK.
[3]Department of Geology and Geophysics, Texas A&M University, College Station, Texas, USA.

8755-1209/10/2009RG000308
Paper number 2009RG000308

impacts of a given size is lower the smaller the size of the impacting body (assuming only small variations in impact velocity for a given planet). Translating extraterrestrial crater size-frequency relationships to the Earth suggests that a 10 m diameter object (iron meteorite) strikes the Earth on average approximately every 4000 years, a 100 m diameter object (stone meteorite) strikes approximately every 5000–40,000 years, and a 1 km diameter object (stone meteorite) strikes every 250,000–1,100,000 years [*Bland and Artemieva*, 2006; *Near-Earth Object Science Definition Team*, 2003].

[4] Direct comparisons between crater populations on the Moon, Mars, and Earth are complicated, however, by the fact that the Earth is protected by a thick, dense atmosphere. For planets with an atmosphere, small meteoroids do not reach the surface with sufficient velocity to form a crater. As they penetrate the gaseous envelope, they are decelerated by atmospheric drag, before exploding and scattering during their final traverse to rain down as fragments (meteorites) at relatively low velocities [*Artemieva and Shuvalov*, 2001; *Chyba et al.*, 1993]. The minimum size of a body that can penetrate Earth's atmosphere without losing a significant amount of its initial velocity is estimated at between 50 and 200 m [*Bland and Artemieva*, 2003; *Chyba et al.*, 1993], depending on composition (iron or stone) and the specific material properties, such as strength and density. The average interval between such events is controversial. *Ward and Asphaug* [2000] estimate that an asteroid ~200–300 m in diameter impacts on Earth approximately every 3000–4000 years. More recent studies predict an average interval for the same impactor size range of approximately 50,000–60,000 years [*Bland and Artemieva*, 2003, 2006].

[5] As discussed above, Earth's impact record does not reflect the estimated impact frequency at Earth's surface, even accounting for the filtering effect of the atmosphere; the paucity of identified impact structures on Earth is due to other reasons. First, in comparison to other planetary objects, Earth is geologically very active. Constant recycling of the Earth's oceanic crust via plate tectonics has erased or altered beyond all recognition the evidence of the majority of terrestrial impact events. In addition, most impact structures that formed on old stable continental shields are heavily eroded and now hardly recognizable as craters. For example, old terrestrial impact structures often lack typical morphological elements seen in extraterrestrial craters, such as bowl-shaped interiors, or flat floors, and raised rims and central peaks. Conversely, many impact structures are covered by sediment that on one hand protects them from erosion and morphological modification but on the other hand removes them from direct observation. Only deep drilling or geophysical exploration can reveal evidence for the existence and morphology of buried impact structures.

[6] The second and perhaps most important reason for the lack of impact structures on Earth is that Earth is the only planet in the solar system where liquid water currently exists on the surface. The presence of a water layer inhibits direct observation of impact structures on the ocean floor and also affects the formation of an impact crater significantly. Oceans cover 70% of Earth's surface, and the unequal distribution between oceans and landmasses (2:1) on the surface of our planet implies that approximately twice as many impacts must have occurred in marine environment than on land throughout much of Earth's history. Despite this, only 15–20 of the approximately 170 known impact craters on Earth are thought to have formed in a marine environment [*Ormö and Lindström*, 2000], and the majority of these are now on land. The relatively small number of known impact structures on the seafloor may be explained, in part, by the young age of the ocean crust in comparison to the continental shields. The oldest ocean crust is approximately only 180 million years old and, therefore, has been exposed to the flux of extraterrestrial bodies impacting the Earth for a much shorter duration than the continental shields.

[7] Another important reason for the lack of impact structures on the seafloor is that the impacting body first has to penetrate through the water column before it can modify the solid strata underneath. Similar to the deceleration effect of the atmosphere, smaller meteoroids (much smaller than the water depth) lose much of their kinetic energy during their traverse of the water layer. In this case, no (or only minor) structural modifications are left behind in the ocean bottom. Evidence of impacts that do not form craters, such as high shock pressure modifications and meteoritic material, have been found in the geological record of the ocean crust; however, relicts of these events are hard to detect. So far, only one locality has been discovered where an oceanic impact occurred without forming a crater: the Eltanin structure in the Bellingshausen Sea, Antarctica [*Kyte et al.*, 1981].

[8] These arguments may explain why the seafloor was less often impacted; however, statistical analyses [*Davison and Collins*, 2007] have shown that the ocean floor should still exhibit a significantly higher crater density than currently observed and, thus, a large number of undiscovered impact structures on the seafloor should exist. The coarse resolution of bathymetric images of the marine basins and insufficient geophysical mapping are probably the main reasons why so few craters have yet been detected. This observation combined with the fact that oceanic impact is the most likely scenario for any future large meteorite impact emphasizes the need to better understand oceanic impacts and their direct and indirect consequences.

[9] Perhaps the most important implication of an oceanic impact is the generation of large waves: impact-generated tsunamis. The generation of such waves may pose an important additional hazard for future impacts over those considered for subaerial impacts [*Collins et al.*, 2005; *Toon et al.*, 1997; *Hills et al.*, 1994]. Quantifying the scale of impact tsunamis is controversial, but the question remains as to whether small bodies (less than ~1 km) might "punch above their weight" by generating large waves that threaten coastal areas a large distance from the point of impact [*Melosh*, 2003; *Ward and Asphaug*, 2003]. In addition, if large waves are generated by impacts, there should be evidence of this in the geological record. Do "megatsunami" deposits exist in the geological record that can be assigned

to impact origin, and if so, can they be used to identify oceanic impact events in Earth history where structural evidence in the ocean floor is lacking or has not yet been discovered? Reconstructing Earth's impact record is of crucial importance both for assessing the frequency of collision events in the past and for better predicting the probability of future impact.

[10] Marine environment impacts differ in several respects from the strike of an asteroid or comet on land because of the water mass involved in the cratering process [*McKinnon*, 1982]. *Ormö and Lindström* [2000] showed that there are unique morphological features of impact craters formed at the ocean bottom. However, there are very few accessible examples of marine target craters that provide information to reconstruct the entire process of an oceanic impact. Experimental studies of hypervelocity impacts into water-covered targets are limited in terms of scale, and extrapolation to larger dimensions has to be done with caution. Numerical modeling is a vital tool in the study of hypervelocity impact processes that, in particular, provides detailed insight into the different stages of an oceanic impact event: the penetration of the projectile through the water column, crater formation and subsequent modification by strong water currents over the seafloor, and the generation of large water waves that propagate away from the impact area.

[11] In this paper we summarize the advances in the study of oceanic impact over the last decades and focus in particular on how numerical models, known as hydrocodes, have improved our understanding of cratering in the oceanic environment and the impact generation of waves. We first give a brief introduction to hydrocode modeling and the codes employed in studies of marine target cratering. We then discuss how a water layer affects the three main stages of the cratering process: (1) the penetration of the projectile through the water column and the generation and propagation of shock waves in water and in the ocean floor, (2) crater growth in water and in the seafloor, and (3) the late stage modification of the crater due to gravitational collapse and water resurge. Section 5 is devoted to the subject of generation and propagation of large waves in the water column propagating away from ground zero. Finally, we summarize the present state of oceanic impact modeling research and highlight interesting avenues for future work.

2. MODELING OF OCEANIC IMPACTS WITH HYDROCODES

[12] Cosmic bodies impact Earth's upper atmosphere at speeds greater than 11 km s^{-1} (the most probable asteroidal encounter velocity is 19.3 km s^{-1} [*Ivanov*, 2007]). A collision at such high speed is referred to as a hypervelocity impact because the impact velocity is many times faster than the speed of sound in water or rock. Hypervelocity impact results in the rapid compression of impactor and target and the generation of a shock wave. The shock wave propagates away from the impact site with an initial speed close to the impact velocity and an initial pressure amplitude of (typically) hundreds of GPa. Despite the large bulk moduli of water and rock, these materials can be compressed to more than twice their original density during the brief passage of the shock wave [*Melosh*, 1982]. Hence, the compressible Navier-Stokes equations must be solved to simulate impact processes. To simulate the propagation of water waves across an ocean, simpler forms of the Navier-Stokes equations for incompressible fluid flow, such as the shallow water equations and so-called Boussinesq equations, can be used.

[13] Besides the governing differential equations of conservation of mass, momentum, and energy, numerical impact models must solve, for each material, an equation of state (EoS) that relates the pressure (the hydrostatic part of the stress tensor), the density and energy (and temperature), and a deviatoric stress model that relates the nonhydrostatic part of the stress tensor to deformation. The accuracy of the EoS is pivotal for the correct treatment of the shock wave compression. Most geological materials are thermodynamically complex and require EoS models that combine empirical data with meaningful thermodynamic assumptions (e.g., the Thomas-Fermi high-pressure limit). Widely used EoS models in impact modeling are the Tillotson EoS [*Tillotson*, 1962], the semianalytical EoS ANEoS [*Thompson and Lauson*, 1972], and the tabular EoS SESAME [e.g., *Lyon and Johnson*, 1992]. The latter two models can account for phase transitions (solid state, melting, and vaporization).

[14] Deviatoric or constitutive models describe the response of a material to deviatoric deformation, the change in shape. For fluids, stress is simply related to the strain rate. For solid geologic materials, on the other hand, deviatoric stress is a complicated function of strain, strain rate, and most importantly the shear strength of the solid material. Material shear strength, which may depend on pressure, temperature, strain, and strain rate, is the limiting stress that a material can support before it breaks (failure) and deforms plastically. Various constitutive models are employed in impact models ranging from simple shear strength models, such as the Drucker-Prager description where shear strength is a linear function of pressure, to complex models that include different styles of failure (brittle versus ductile) and strength degradation (strain softening and thermal softening). For a more detailed description of material models used in hydrocode modeling, see, for example, *Ivanov et al.* [1997] or *Collins et al.* [2004].

[15] Computer codes that numerically solve systems of equations described above are commonly called hydrocodes [*Anderson*, 1987; *Benson*, 1992; *Pierazzo and Collins*, 2004], although a more appropriate term for today's codes that include complicated deviatoric stress models is shock physics codes [*Pierazzo et al.*, 2008]. The numerical simulations of oceanic impact events to which we refer to in this paper were conducted using a number of different hydrocodes: SOVA [*Shuvalov*, 1999], CTH [*McGlaun and Thompson*, 1990], SAGE [*Gittings*, 1992], SALEB/iSALE [*Ivanov et al.*, 1997; *Wünnemann et al.*, 2006], and AUTODYN [*Century Dynamics, Inc.*, 2003]. Although the system of equations that they solve is the same, different hydrocodes use different approaches to discretize the

equations (e.g., finite difference method or finite element method and Lagrangian or Eulerian descriptions), to discretize the spatial domain (e.g., fixed mesh or adaptive mesh), and to stabilize the solution. More importantly, hydrocodes differ in the level of sophistication in the material models (bulk and deviatoric). It is beyond the scope of this review to describe even the most important differences between these codes and how these differences may influence the results. Nonetheless, it is important to understand the relative accuracy of these codes and hence the uncertainty associated with all hydrocode simulation results. *Pierazzo et al.* [2008] presented the first results from an international project to benchmark and validate impact hydrocodes, including all those mentioned above. This work demonstrated that even for idealized impacts the variability between hydrocodes in calculating peak shock pressure as a function of distance can be as much as 10%–20%. Hydrocode simulations designed to reproduce crater growth observed in small-scale laboratory impact experiments produced results that agreed with experimental data to within 10%, which was similar to the intercode variability. Thus, results presented in this paper that are derived from different hydrocodes likely have an uncertainty of around 10%–20%.

3. PENETRATION OF THE WATER COLUMN AND GENERATION OF SHOCK WAVES

[16] A cosmic body that collides with Earth must first penetrate the atmosphere before it reaches the surface of an ocean. Depending on the size and velocity of the impacting body, the passage through Earth's gaseous envelope results in deceleration, deformation, and/or disruption of the projectile. As our focus here is on the effect of the water layer, not the atmosphere, we refer to more specialized literature on atmospheric entry of meteoroids [*Chyba et al.*, 1993; *Collins et al.*, 2005; *O'Keefe and Ahrens*, 1982] and the breakup of small projectiles [*Artemieva and Shuvalov*, 2001; *Bland and Artemieva*, 2003]. In some regards, the processes acting on an impactor as it traverses the atmosphere and water column are mechanically and thermodynamically similar, and the same physical descriptions apply. However, while the density of the atmosphere decreases exponentially with height above the Earth's surface, the air-water interface is a sharp discontinuity in density. Thus, impacts into water also share many characteristics of impacts into dense solids [*Melosh*, 1989]. For a detailed description of impacts in solid targets the interested reader is referred to the two comprehensive texts [*French*, 1998; *Melosh*, 1989]. In sections 3.1 and 3.2, we describe the early stages of a marine impact: the penetration of the impactor through the water layer and the concurrent generation and propagation of the shock wave in water.

3.1. Deceleration of the Impactor by the Water Layer

[17] The deceleration of the impactor during traverse of the water column is a complex process that depends on the velocity, density, and composition of the impacting body. However, a simplified equation of motion that accounts for the drag of the surrounding water on the penetrating impactor can be derived by assuming that the impactor is spherical, that it does not deform, and that both the impactor and the fluid are incompressible [e.g., *O'Keefe and Ahrens*, 1982]:

$$\frac{4}{3}\pi a^3 \delta \frac{dU}{dt} = -C_D \pi a^2 \rho U^2 \tag{1}$$

In this equation, a is the impactor radius, δ is the impactor density, U is the impactor velocity, ρ is the fluid density, and C_D is the drag coefficient (0.877 for a rigid body in supersonic regime [*Landau and Lifshitz*, 1959]). Assuming that the impactor travels in a straight line (in the x direction) and using the substitution $U = dx/dt$, equation (1) can be integrated from $U = U_0$ at $x = 0$ to U at $x = d$, where U_0 is the initial velocity and d is the penetration depth. Thus, the kinetic energy E of the impactor normalized by its initial kinetic energy E_0 can be written as a function of penetration depth d over impactor diameter $L = 2a$:

$$\frac{E}{E_0} = \frac{U^2}{U_0^2} = \exp\left(-3C_D \frac{\rho}{\delta}\frac{d}{L}\right). \tag{2}$$

[18] It is worth reiterating that several gross simplifications are made in the derivation of this equation for the deceleration of an impactor in water, which is often referred to as the supersonic drag approximation (SDA). These include the assumptions that the generation and propagation of the shock wave in the water can be neglected and that the impactor does not compress, deform, or lose mass by ablation. Only the very last of these assumptions is valid. *O'Keefe and Ahrens* [1982] showed that only a small fraction of the mass of the projectile is ablated by comparing the time it would take the impactor to penetrate the entire ocean with the time it would take to ablate the bolide [*O'Keefe and Ahrens*, 1982, equation 14].

[19] Hydrocode modeling provides a method to more accurately determine the deceleration and kinetic energy loss of an impacting body as it travels through a fluid. In such models many aspects contributing to the deceleration are taken into account: the drag force of the water, shock compression and heating of the impacting body and the surrounding medium, and deformation of the bolide. The first modeling studies that focused specifically on the traverse of the projectile through a water layer were carried out by *O'Keefe and Ahrens* [1982], who employed a hydrocode developed by *Dienes and Walsh* [1970]. For a 15 km s^{-1} impact their results are in good agreement with equation (2) to a penetration depth of one projectile radius. For larger penetration depths the energy loss in the models is less than predicted by the SDA; for example, in the model at a penetration depth of 14 impactor radii the projectile retained almost 10% of its initial total energy, while according to the SDA essentially all the projectile's kinetic energy is transferred to the water column (Figure 1). However, *O'Keefe and Ahrens* [1982] account for the total energy (kinetic

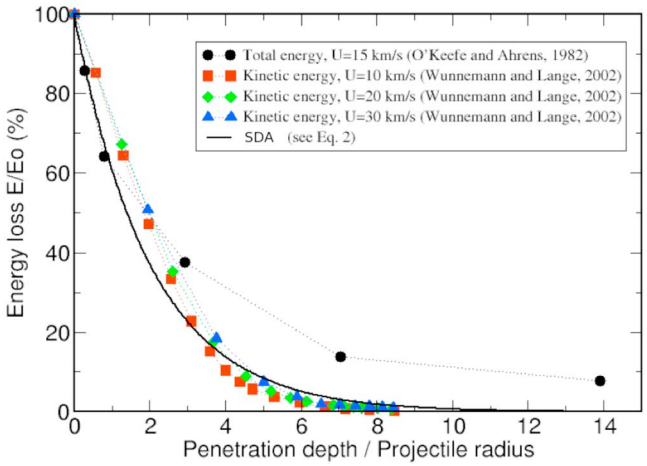

Figure 1. Percentage of the remaining energy of the impactor versus normalized penetration depth. SDA marks the supersonic drag approximation given in equation (2). Note that the *O'Keefe and Ahrens* [1982] model considers the total energy (kinetic plus internal), while the *Wünnemann and Lange* [2002] models only account for the kinetic energy.

plus internal energy) of the projectile, while the SDA considers the kinetic energy only (the projectile is assumed to be incompressible). This may explain the difference between models and SDA for greater penetration depths as the projectile gets highly compressed.

[20] Using an early version of the SALE hydrocode that was specifically adjusted to modeling impact processes, *Wünnemann and Lange* [2002] showed that the supersonic drag approximation is an adequate first-order approximation for the deceleration of a stony impactor up to a penetration depth of ~4 impactor radii (Figure 1). As the impactor penetrates further, it spreads laterally (so-called pancaking), which increases the drag on the impactor and decelerates it more rapidly than predicted by the SDA. At the same time, the impactor is released from high pressure and begins to vaporize; the reduction in density and increase in volume both increase the effect of the drag force and act to slow the impactor further. If these processes combine to decelerate the impactor, it may be essentially stopped by the time it has traveled several impactor diameters through the water. However, the "stopping" distance of an impactor traversing a water layer does not just depend on impactor diameter.

[21] Figure 2 shows the results of several new hydrocode simulations with Impact-SALE (iSALE) of impactor penetration through a water layer compared with the supersonic drag approximation. (The code iSALE is a further code extension to the SALE code that is developed in parallel to the generally very similar SALEB code [e.g., *Ivanov et al.*, 1997]. The most important extension here is that the code can model up to three different materials and vacuum in any computation, while the older versions (e.g., SALE described by *Wünnemann and Lange* [2002]) were capable of dealing with two materials only.) Results are shown for two projectile densities (granite, 2700 kg m^{-3}, and iron, 7800 kg m^{-3}) and two initial velocities (5 km s^{-1}, typical of laboratory experiments in water, and 15 km s^{-1}, typical of impacts on Earth). Also illustrated are the SDA for both impactor densities (solid lines). In all cases, the SDA is a reasonable approximation for the deceleration of the impactor for penetration depths up to ~2 projectile diameters L. At greater penetration depths, both 5 km s^{-1} impactors decelerate much more rapidly than predicted by the SDA because of lateral spreading (pancaking) of the impactor. The faster impactors appear to follow the SDA more closely; however, this is misleading. In fact, as these impactors penetrate the water, they first pancake, which results in a more rapid deceleration than predicted by the SDA. Subsequently, the sides of the squashed impactor fold in, or are sucked in (see also Figure 5), behind the front of the impactor to form a high-speed jet of impactor material, with a smaller cross-sectional area than the original body. Thus, jet formation may reduce the rate of deceleration relative to the SDA. Therefore, the deceleration curve moves above the SDA curve in Figure 2. With continuing penetration, the jet may pancake again so that the rate of deceleration is again greater than predicted by the SDA. These different phases of deceleration are highlighted on the 15 km s^{-1} iron impactor curve and are also evident for the 15 km s^{-1} granite impactor.

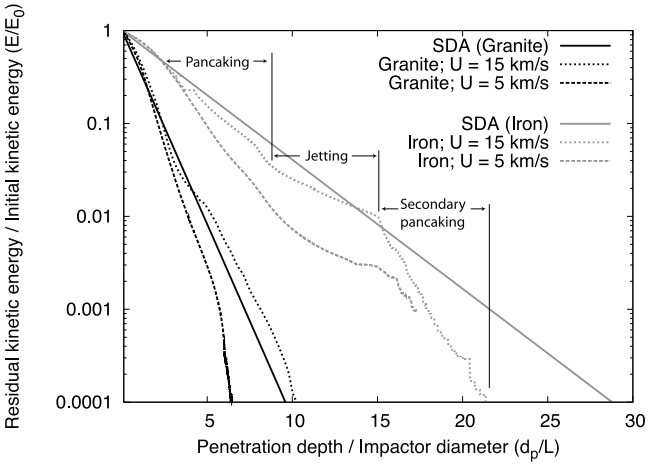

Figure 2. Impactor deceleration as a function of penetration depth in water. The residual kinetic energy of the impactor as a fraction of its initial kinetic energy E/E_0 is plotted against the normalized penetration depth (penetration depth divided by impactor diameter). Shown are curves for the supersonic drag approximation (SDA) for two impactor densities, and the results of hydrocode simulations are shown for two impactor densities and initial velocities. See text for details. The SDA assumes that the impactor does not deform during penetration; however, hydrocode simulation results suggest that the impactor may flatten (pancaking), form a narrow jet (jetting), and then flatten again (secondary pancaking), depending on the density and initial velocity of the impactor.

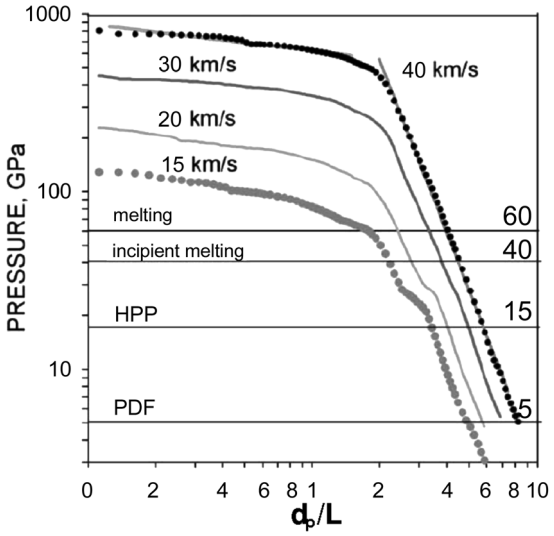

Figure 3. Shock pressure decay in water, based on SOVA simulations of deep water impacts. Peak shock pressure is plotted against normalized water depth d_p/L. Results are shown for four different impact velocities. Horizontal lines mark critical pressures for various shock metamorphic effects in quartz (see text for details). Shock pressure decay is proportional to $(d_p/L)^{-0.15}$ inside the isobaric core and proportional to $(d_p/L)^{-3}$ in the far field. HPP stands for high-pressure phase, and PDF means planar deformation features. Reprinted from *Artemieva and Shuvalov* [2002, Figure 2], copyright 2002, with permission from Elsevier.

3.2. Shock Wave Generation and Propagation in Water

[22] During the initial collision of a body with the water surface, the impactor and a similar volume of water are compressed to very high density, which raises the pressure and temperature of this material and generates a shock wave at the impactor-water interface. This shock wave propagates away from the contact zone, briefly raising the density, pressure, and temperature of the water in its path. The amplitude of the excursion decays with distance traveled by the shock wave. Behind the shock wave, a rarefaction wave generated by reflection of the shock wave at the free surface (i.e., the rear of the projectile and the air-water interface) releases the compressed material from its high-pressure state. Shock wave compression is irreversible, whereas decompression is reversible; hence, the passage of the shock wave results in a net increase in temperature (internal energy and entropy) and particle velocity in the water [*Melosh*, 1989]. If the shock is strong enough, and the release conditions favorable, the net gain in internal energy can irrevocably change the physical state of the target material by solid-state phase transition, melting, or vaporization.

[23] The impact-generated shock wave propagates away from the contact zone ahead of the decelerating impactor and reaches the ocean floor before the impactor. The decay of peak shock pressure in water with depth was quantified by *Artemieva and Shuvalov* [2002], who simulated impacts of a stony projectile into deep water at various impact velocities (Figure 3). As for all materials, shock decay can be separated into two regions: a proximal zone of near-constant high pressure, often referred to as the isobaric core, and a far-field region where the pressure drops rapidly with distance. The size of the isobaric core, the peak shock pressure in the isobaric core, and the rate of pressure decay with distance in the far field all depend on the material properties of the impactor and target and the impact velocity. For impacts into water, *Artemieva and Shuvalov* [2002], using the SOVA hydrocode, showed that the isobaric core extends to a depth of approximately two impactor diameters. For an impact velocity of 20 km s^{-1}, peak pressures in the isobaric core is approximately 250 GPa near the surface and decays proportional to $(d_p/L)^{-0.15}$ to ~100 GPa at a depth $d_p \approx 2\ L$. In the far-field region ($d_p > 2\ L$) peak pressure decays more rapidly, proportional to $(d_p/L)^{-3}$, to ~5 GPa at a depth of six impactor diameters.

[24] *Artemieva and Shuvalov* [2002] used their numerical results to determine the effect of water depth on shock modification of the seafloor. Shock wave compression of >5 GPa can cause unique, permanent modifications in rocks and minerals (shock metamorphism). These modifications are used to unequivocally identify impact events and to calibrate the shock wave amplitude the material was exposed to (shock wave barometry [e.g., *Stöffler*, 1972]). For quartz a peak shock pressure of ~5 GPa results in planar deformation features, a shock pressure of 15 GPa results in a solid-state high-pressure phase transition, incipient melting occurs for shock pressures above 40 GPa, and complete melting occurs for shock pressures above 60 GPa. By assuming that the pressure of the shock wave transmitted to the seafloor is approximately the same as the pressure at the same depth in water, *Artemieva and Shuvalov* [2002] used the pressure decay in deep water to estimate the critical sea depths for which shock effects in quartz on the seafloor would not be observed (Figure 3). They estimated that no significant melting of the seafloor should occur if the water depth is greater than two impactor diameters for an impact at 15 km s^{-1} and four impactor diameters for an impact at 40 km s^{-1}. No shock effects ($P < 5$ GPa) occur at all if the water depth is 5–8 times the impactor diameter (for impact velocities of 15–40 km s^{-1}). Similar results were obtained by *Wünnemann and Lange* [2002] using an early version of the SALE hydrocode that was specifically adjusted to modeling impact processes.

[25] If the impactor is slowed so much that it does not strike the seabed, shock modification of the seafloor may provide the only permanent evidence of impact. The Eltanin structure in the Bellinghausen Sea, Antarctica [*Kyte et al.*, 1981], is the only known example of such an impact. There is no crater-like structure visible in the ocean bottom, but other modifications of the benthic strata were observed that are discussed in section 4.6.

4. CRATERING IN THE OCEAN AND SEAFLOOR

[26] Crater formation in the water column and the seafloor may be viewed as separate processes until they merge

during late stage modification. While the water column always returns to its preimpact level, the seafloor may undergo permanent deformation due to the strength of the underlying strata. The resulting crater morphologies are similar to crater structures in continental targets and on planetary surfaces; however, interaction with the water layer during late stage modifications can cause important structural differences characteristic of marine impact craters. In sections 4.1–4.6 we describe the cratering process and how crater dimensions depend on the impact energy and the thickness of the water layer relative to the size of the impactor.

4.1. Crater Formation in Water and the Seafloor

[27] Conventionally, the crater formation process can be subdivided into a sequence of different stages: (1) the contact and compression stage, (2) the excavation stage, and (3) the modification stage. The separation into different stages characteristic for specific processes was first suggested by *Gault et al.* [1968] and applies equally to cratering in the water column and in the seafloor; however, it is important to note that the stages grade into one another. Moreover, there may be a short but significant hiatus between the onset of crater formation in the seafloor and in the water layer. Here we only provide a brief overview and refer to *Melosh* [1989] for a more elaborate description.

[28] First, during the contact and compression stage the impactor collides with the target (water surface or seafloor) and generates a shock wave as was described in section 3. Second, during the excavation stage, the shock wave propagates through the target (water layer or seafloor), transferring energy and momentum to the target and establishing an excavation flow that opens up a deep bowl-shaped crater.

[29] Eventually, crater growth is halted when insufficient kinetic energy remains to displace the target against its own weight (gravity-dominated cratering) or against the cohesive strength of the target material (strength-dominated cratering). Since water has no strength the latter may apply only to crater formation in the seafloor. The resulting crater at the end of excavation stage is called transient crater. Notably, the transient crater may be reached later in the water column than in the underlying strata because of smaller density and the lack of strength in the water.

[30] Finally, the deep crater in the water column is not stable in Earth's gravity field and eventually collapses. The collapse of the transient crater in the water column causes water flow along the seafloor that will be discussed in section 4.6 and leads to the generation of large waves, described in section 5.

[31] In a similar way, the collapse of the transient crater in the seafloor may take place if the target material is weak or the weight of the displaced material is large. The amount and extent of collapse depend sensitively on the strength properties of the benthic strata and the dimensions/extent of the transient crater in the seafloor. Smaller craters (<2–4 km for terrestrial craters [*Dence*, 1965]) experience only minor gravity-driven modification, such as slumping of oversteepened crater walls. The final crater structure of so-called simple craters is similar to the size and shape of the transient crater. Larger transient craters (greater than ~4 km for terrestrial craters [*Dence*, 1965]) are unstable in the given gravity field. The deepest point of the cavity uplifts to form a central peak or ring surrounded by a flat crater floor, while at the same time, concentric blocks of the crater wall slump inward, leading to the formation of a terraced rim zone. The resulting crater morphology corresponds to so-called complex craters. Note that in the case of complex crater morphology the final crater is much larger than the transient crater. The size of the final structure cannot be straightforwardly related to the kinetic energy of the impactor. As discussed in section 4.2, the water layer affects crater formation in the seafloor and complicates the prediction of the resulting crater size and morphology for a given impactor size.

4.2. Crater Scaling in Water and Rock

[32] Numerical impact models and laboratory impact experiments provide data relating the size of a crater to the properties of the impactor and target used in the experiment or model. Scaling laws combine results from models and experiments and allow their extrapolation to impactor and target conditions beyond those studied. A well-developed suite of scaling laws in impact cratering are the "Pi group" scaling laws, which are derived using dimensional analysis under the assumptions that an impact may be adequately represented by a point source of momentum and energy [e.g., *Holsapple*, 1993; *Holsapple and Schmidt*, 1987]. Such analyses predict power law relationships between crater size and the appropriate measure of the impactor/target conditions. For impacts into water, the appropriate measure is (to within a numerical factor) the inverse Froude number (typically called the gravity-scaled source size, π_2), which is the ratio of a lithostatic pressure $\rho g a$ to the initial dynamic pressure generated by the impactor ρU^2. In terms of π_2, the cratering efficiency in water (the maximum volume of the crater, times the water density ρ, divided by the projectile mass m) is given by

$$\frac{\rho V}{m} = 1.6\left(3.22\frac{ga}{U^2}\right)^{-0.65} \Rightarrow \pi_V = C_V \pi_2^{-0.65}, \tag{3}$$

which can be rearranged to give

$$V = 0.75\left(\frac{\delta}{\rho}\right)^{1/3} a^{2.35} g^{-0.65} U^{1.3}. \tag{4}$$

In equation (4) δ is the density and a is the radius of the projectile, and V is the crater volume. Quite amazingly, this expression has been shown to hold over 3 orders of magnitude in velocity, with conditions ranging from ball-dropping experiments at speeds of 1–20 m s^{-1} to light gas gun experiments at speeds up to 6 km s^{-1} [*Holsapple*, 1993]. It is also in good agreement with numerical models of impact cratering in water for realistic impact velocities of ~18 km s^{-1} and crater dimensions of several hundred meters to tens of kilometers. Figure 4 shows the "gravity-scaled size" of an impact event π_2 versus scaled crater efficiency

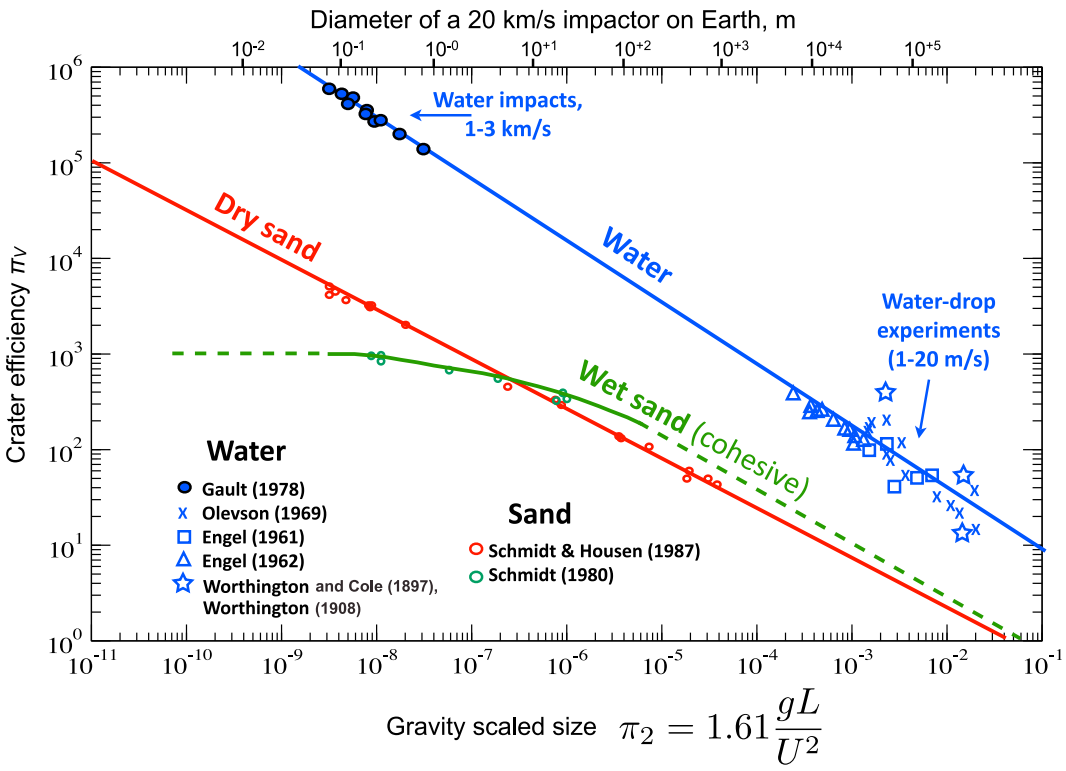

Figure 4. Cratering efficiency as a function of gravity-scaled size. Results are shown for vertical laboratory impact experiments in water and dry and wet sand. All data are taken from references indicated in Figure 4. Lines show the predicted crater efficiency according to scaling laws [e.g., *Holsapple*, 1993].

π_V over several orders of magnitude. Similar power law relationships are given for the scaled crater diameter $\pi_D = D(\rho/m)^{1/3}$ and scaled crater depth $\pi_d = d(\rho/m)^{1/3}$, where D is the crater diameter and d is the crater depth [e.g., *Housen and Holsapple*, 2003].

[33] The same scaling laws are also applicable for crater formation in rocks or granular materials. However, crater growth in these materials is also affected by strength (cohesion and friction). Therefore, different scaling parameters, C_V and γ, must be used in equation (3) for different target materials (see, for example, *Holsapple and Housen* [2007] and *Schmidt and Housen* [1987] for experimentally derived scaling parameters and *O'Keefe and Ahrens* [1999], *Wünnemann and Ivanov* [2003], and *Elbeshausen et al.* [2009] for modeling-derived scaling parameters). (Note that equations (3) and (4) do not apply for small laboratory-sized craters in cohesive materials, such as intact rock or metals. In this case, the crater dimensions are controlled by the high cohesion of the material rather than by gravity and friction. For more details on crater scaling, see, e.g., *Holsapple* [1993].) These scaling laws apply only to uniform, single-material targets and cannot be used to estimate the dimensions of a crater on the seafloor, for instance.

4.3. Cratering on the Seafloor

[34] Numerical impact models show that crater growth in the seafloor is driven both by the passage of the shock wave transmitted from the water above and, moments later, by the penetration of the impactor. For impacts into shallow water, the shock wave and impactor arrive at the seafloor almost simultaneously for typical impact velocities, and the shock energy is focused over a small region of the seafloor (Figure 5a). In this case, the acceleration of the seafloor material is continuous, resulting in downward and outward crater growth. The size of the crater in the seafloor depends on the combination of the strength of the shock wave transmitted to the seafloor and the residual kinetic energy of the impactor after traverse of the shallow water layer. In impacts into deep water, the shock wave may reach the seafloor seconds before the impactor, and the incident shock wave interacts with the seafloor over a much broader region (Figure 5b). In this case, impact-induced deformation of the seafloor includes an initial shock-driven phase of broad downward displacement. Impact-induced deformation may be followed, or superimposed, by more localized deformation due to the penetration of the impactor if the impactor maintains a sufficiently large velocity during its traverse of the water layer. In these events, the size of the broad depression in the seafloor depends on the strength of the shock wave transmitted to the seafloor, whereas the size of the penetration crater depends on the residual kinetic energy of the impactor. Whether such deep water "cratering" occurs, and if it does, the water depth at which it occurs, depends critically on the details of the impactor's penetration of the water layer.

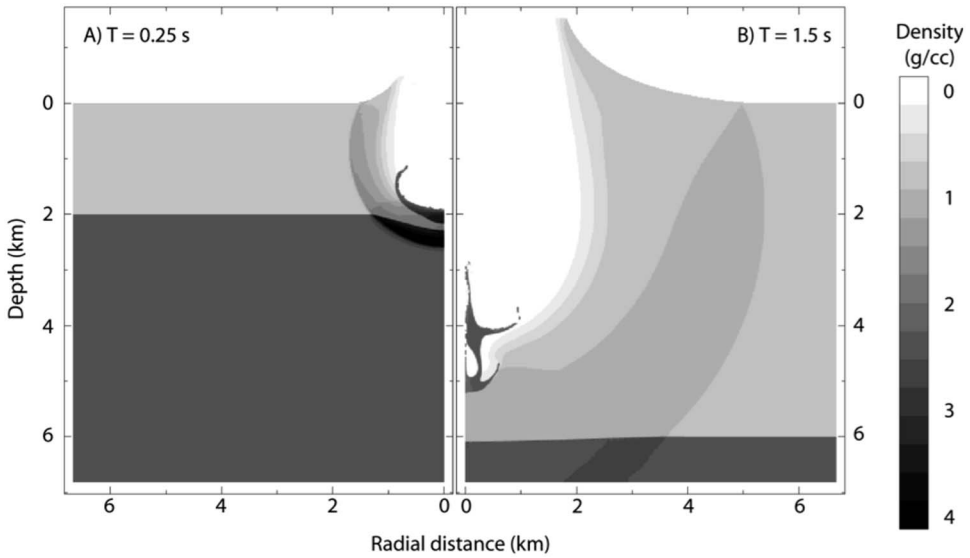

Figure 5. Comparison of the initiation of (left) shallow water and (right) deep water "cratering." Both images show contours of density in the seafloor and the water above, at a time shortly after the shock wave is transmitted to the seafloor and initiates cratering. The impactor diameter and velocity in both cases were 1 km and 15 km s^{-1}. In Figure 5 (left), the water depth is twice the impactor diameter (shallow); in Figure 5 (right), the water depth is 6 times the impactor diameter (deep). In the shallow water case, the impactor reaches the seafloor almost at the same time as the shock wave; in the deep water case, the shock wave reaches the seafloor and begins to deform it well before the impactor reaches the seafloor.

4.4. Suppression of Seafloor Cratering Due to a Water Layer

[35] The critical ratio of water depth to projectile diameter, above which no crater will form on the seafloor, depends on the water depth required to reduce the inertial stress of the decelerating impactor ($\sim\delta U^2$) to less than the effective strength of the seafloor. The results in Figure 2 demonstrate that this depends on the density of the impactor, the initial velocity of the impactor, and the strength of the seafloor. Because of the number of factors involved, published estimates of the critical water depth required to suppress cratering in the seafloor vary, as summarized in Table 1. *Shuvalov* [2002] suggested a very low critical water depth of ~4 projectile diameters L, on the basis of simulations of 200 m diameter, 15 km s^{-1} impactors. However, in this case the seafloor was assigned a very high strength, of 100 MPa, which is inappropriate for large-scale impacts. Indeed, the simulations by *Shuvalov and Trubetskaya* [2002], which employed a more realistic strength model for the seafloor, showed cratering for a 1 km diameter impactor into a 4 km deep ocean.

[36] *Davison and Collins* [2007], using the iSALE hydrocode with a strength model appropriate for impacts in crystalline rocks, showed that the critical water depth to suppress cratering was ~6–8 L for impacts of 0.1, 0.5, and 1 km diameter bodies, at 15 km s^{-1}. *Milner et al.* [2007] used the AUTODYN hydrocode to examine the effect of several impactor variables on the critical water depth required to suppress cratering. In all their models the target was assigned typical static strength parameters for sandstone (again, these parameters imply an unrealistically high strength for the target rocks in large-scale impacts). Nevertheless, the AUTODYN calculations predicted that a water depth of 7–9 L was required to suppress cratering for impact of a 1 km diameter basalt impactor at 20 km s^{-1}, which is in good agreement with the results of *Davison and Collins* [2007] for similar impact parameters. *Milner et al.* [2007] also showed that for an impactor diameter of 1 km and an impact velocity of 20 km s^{-1}, the critical water depth to suppress cratering increases with impactor density up to 17.5–20 L for δ = 7800 kg m^{-3} (steel). Moreover, for an impactor density of 7800 kg m^{-3}, the critical water depth was observed to depend on both impact velocity and, for very small impactors, impactor diameter.

[37] Laboratory experiments have also quantified the critical water depth required to suppress cratering in the benthic surface (Table 1). The pioneering experiments of *Gault and Sonett* [1982] showed that cratering in wet sand, below a water layer, was suppressed for a water depth of 14–20 L. In these experiments, the projectiles were 3.2 mm diameter Pyrex spheres, and the impact velocity was 2.5 km s^{-1}. *Milner et al.* [2007] and *Baldwin et al.* [2007] performed experiments of 1 mm diameter steel spheres impacting at ~5 km s^{-1} into water-over-granite and water-over-sandstone targets, respectively. They determined a critical water depth of 8–10 L for granite; 10–12 L for dry sandstone; and >12 L for slightly weaker, wet sandstone. AUTODYN simulations performed to reproduce the conditions of the impact experiments into sandstone targets showed good agreement with experiments in terms of critical water depth [*Milner et al.*, 2007].

TABLE 1. Summary of the Critical Water Depth Required to Suppress Cratering as Determined From a Range of Numerical Modeling and Experimental Studies

Projectile					
Diameter L	Velocity v_i (km s^{-1})	Type and Density ρ_i (g cm^{-3})	Target Type	Critical Water Depth	Reference
			Numerical Simulations		
200 m	15	Granite (2.68)	Granite ($Y \approx 100$ MPa)[a]	~4	SOVA: *Shuvalov* [2002]
100 m	15	Granite (2.68)	Granite (including damage)[b]	>8	iSALE: *Davison and Collins* [2007]
500 m	15	Granite (2.68)	Granite (including damage)[b]	6–8	iSALE: *Davison and Collins* [2007]
1 km	15	Granite (2.68)	Granite (including damage)[b]	6–8	iSALE: *Davison and Collins* [2007]
1 mm	5	Steel (7.8)	Sandstone	8–8.5	AUTODYN[c]: *Milner et al.* [2007] and *Baldwin* [2008]
1 m	5	Steel (7.8)	Sandstone	6–7	AUTODYN[c]: *Milner et al.* [2007] and *Baldwin* [2008]
1 km	5	Steel (7.8)	Sandstone	6–6.5	AUTODYN[c]: *Milner et al.* [2007] and *Baldwin* [2008]
1 km	10	Steel (7.8)	Sandstone	9–10	AUTODYN[c]: *Milner et al.* [2007] and *Baldwin* [2008]
1 km	20	Steel (7.8)	Sandstone	17.5–20	AUTODYN[c]: *Milner et al.* [2007] and *Baldwin* [2008]
1 km	20	Dunite (3.79)	Sandstone	9–10	AUTODYN[c]: *Milner et al.* [2007] and *Baldwin* [2008]
1 km	20	Basalt (2.86)	Sandstone	7–9	AUTODYN[c]: *Milner et al.* [2007] and *Baldwin* [2008]
1 km	20	Sandstone (1.99)	Sandstone	3–4	AUTODYN[c]: *Milner et al.* [2007] and *Baldwin* [2008]
			Laboratory Experiments		
3.2 mm	2.5	Pyrex (2.3)	Sand (wet)	14–20	*Gault and Sonett* [1982]
1 mm	5	Steel (7.8)	Granite	8–10	*Milner* [2007]
1 mm	5	Steel (7.8)	Sandstone (wet)	>12	*Baldwin et al.* [2007]
1 mm	5	Steel (7.8)	Sandstone (dry)	>10	*Baldwin et al.* [2007]

[a]Cratering flow was arrested when velocity in the seafloor was less than 200 m s^{-1}; this corresponds to an inertial stress ≈100 MPa.
[b]The strength model used in the iSALE simulations is described by *Collins et al.* [2004]. The target is weakened relative to standard strengths by damage, temperature, and acoustic vibrations.
[c]The strength model used in AUTODYN was an elastic-plastic Drucker-Prager model. Crater diameters in the AUTODYN simulations were determined on the basis of the extent of damage in the target, not the dimensions of the physical depression in the seafloor.

4.5. Effect of Water Layer Thickness on Crater Size

[38] Hydrocode simulations in comparison with observations at terrestrial impact craters formed in marine environment [*Ormö et al.*, 2002] and laboratory experiments have also been used to quantify the reduction in transient crater size in the seafloor with increasing water depth. Figure 6 shows the maximum depth of the crater formed in the benthic surface as a function of h/L, relative to the maximum depth of crater when no water layer is present. It includes results from a number of models and experiments that assumed different impactor and target properties. In general, crater depth decreases approximately linearly with increasing water depth. The discrepancies between trends again reflects the variation in the efficiency with which impactors of different initial velocity and density penetrate the water layer, as well as the variation in benthic target strength. The discrepancy between the numerical simulation results of *Shuvalov* [2002] and *Davison and Collins* [2007] is probably due to the difference in target strength; impact velocity and impactor size were the same or very similar in both studies. Similarly, the only difference between the experiments of *Milner* [2007] and *Baldwin et al.* [2007] was the type of rock used for the underlying target (granite versus wet and dry sandstone). Thus, the differences between these data are likely a consequence of the decrease in strength from granite (high strength) to dry and then wet (low strength) sandstone. The discrepancy between these rock target data and the wet sand data from *Gault and Sonett* [1982] may also be due to the low strength of wet sand relative to rock; however, these experiments also differ substantially from those by *Milner* [2007] and *Baldwin et al.* [2007] in terms of impactor size, density, and velocity.

[39] Of utmost importance for relating the results presented in Figure 6 to terrestrial cratering is the difference between the trends suggested by the models and those suggested by the experiments. In general, the numerical model results [*Shuvalov*, 2002; *Davison and Collins*, 2007] suggest a steeper decay of crater size with increasing water depth than observed in the experiments. Besides the strength of the seafloor material, the main differences between the

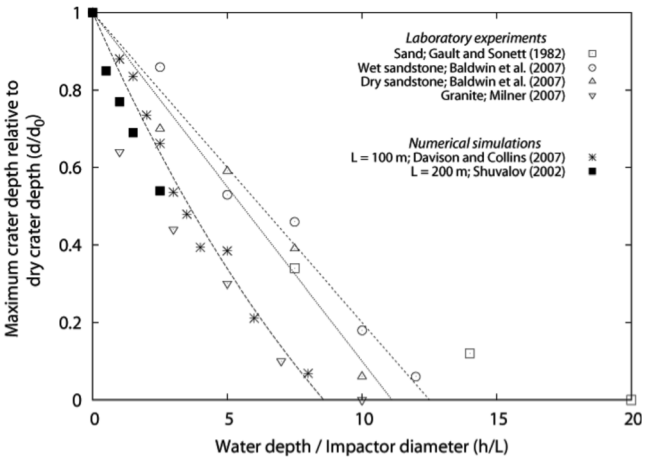

Figure 6. Maximum crater depth in the seafloor, normalized by the maximum crater depth when no water layer is present (dry crater depth), as a function of the ratio of water depth to the impactor diameter h/L. Results are shown from several hydrocode modeling studies and laboratory experiments. The differences between these curves are due to a combination of impactor (size, velocity, and density) and target (strength) differences.

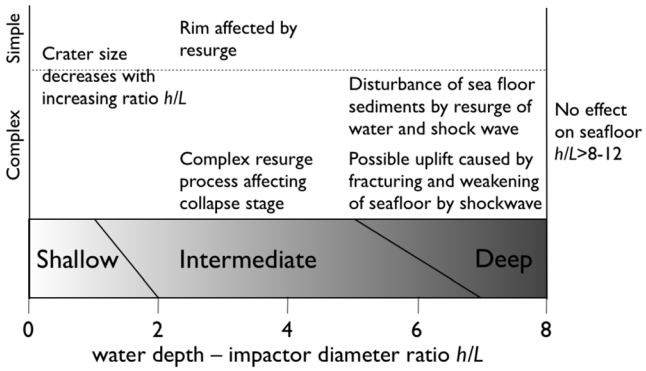

Figure 7. Diagram summarizing the influence of a water layer on the cratering process depending on crater size (vertical axis) as a function of the water depth-impactor diameter ratio h/L (horizontal axis). Three regimes (shallow, intermediate, and deep water impacts) of qualitatively different behavior can be distinguished (modified after *Davison and Collins* [2007]).

models and water-over-rock experiments were in the impact velocity (15 km s^{-1} in the models versus 5 km s^{-1} in the experiments), the impactor density (2700 kg m^{-3} versus 7800 kg m^{-3}), and the impactor diameter (~0.1–1 km versus 1 mm). If rate-dependent processes are not important, the results should be independent of projectile size. As discussed in section 3.1, impactor deceleration by the water layer is more efficient when the initial impact velocity is low and when the impactor density is low. In addition, if the seafloor material has a higher strength, the critical water depth required to suppress cratering will be smaller. Thus, the steeper decay of crater size with water depth predicted by the numerical models of oceanic cratering, relative to the results from small-scale laboratory experiments, is likely due to the lower impactor density used in the models. Hence, the numerical model results probably provide a more realistic estimate of the effect of water depth on crater size for typical asteroid impacts on Earth.

4.6. Crater Modification Due to Gravity Collapse and Water Resurge

[40] As described in section 4.1, transient craters collapse under the influence of gravity; the amount of modification depends on the size of the transient crater. Hence, the presence of a water layer, which suppresses transient crater formation in the benthic target, has a fundamental effect on the morphology of the final crater in the seafloor. Additionally, as water flows back into the cavity, the crater rim and the uppermost strata may be affected by return flow (resurge). Many numerical modeling studies have examined how crater collapse is affected by the presence of a water layer and how resurging water may further modify crater morphology [*Lindström et al.*, 1996, 2005; *von Dalwigk and Ormö*, 2001; *Shuvalov*, 2002; *Shuvalov et al.*, 2002, 2005; *Shuvalov and Trubetskaya*, 2002; *Wünnemann and Lange*, 2002; *Collins and Wünnemann*, 2005; *Davison and Collins*, 2007; *Kenkmann et al.*, 2009]. These results provide insight into how marine target complex craters may differ from their counterparts on land.

[41] *Shuvalov* [2002], *Shuvalov and Trubetskaya* [2002], *Ormö et al.* [2002], and *Davison and Collins* [2007] investigated the effect of water depth on seafloor crater formation for a range of impact scenarios. In each of these studies the seafloor was modeled as a single material with a strength appropriate for crystalline rocks or stronger. Results from these and other studies suggest that three regimes of oceanic impact exist (see Figure 7): (1) shallow water impact (SWI), (2) intermediate water impact, and (3) deep water impact (DWI). The transition between these regimes depends on the size of the crater and the ratio of the water depth to impactor diameter (h/L), although the exact definition of the transitions varies between studies. Figure 8 shows

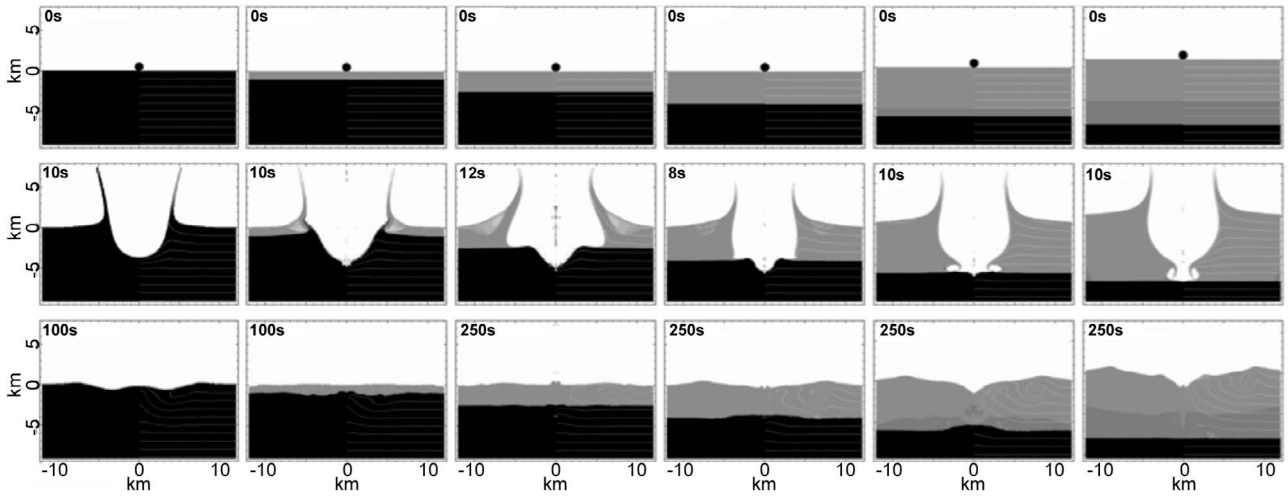

Figure 8. Snapshot series (rows) of numerical models of crater formation for a 1 km diameter impactor for different water depths (columns) with R = 0, 1, 2.5, 4, 6, and 8. The impact velocity was 15 km s^{-1}. (top) The initial state, (middle) the point when the maximum depth of the cavity is reached, and (bottom) the final state. Shading is density. Reprinted from *Davison and Collins* [2007, Figure 2], copyright 2007, with permission from John Wiley.

an example of numerical model results that qualitatively illustrate the effect of water depth on crater formation in the seafloor for a 1 km diameter asteroid striking at 15 km s^{-1} [*Davison and Collins*, 2007].

4.6.1. Shallow Water Impact Regime

[42] In shallow water impacts the effect of the water layer on the impact process is minimal: crater size is only slightly reduced, and the morphology of the final crater is very similar to the equivalent size crater on land. Evidence for water resurge may exist in the form of minor rim modification and crater infilling and depends critically on the strength of the uppermost seafloor. According to *Shuvalov* [2002] and *Shuvalov and Trubetskaya* [2002] the shallow water regime occurs for $h/L < 1$. *Davison and Collins* [2007] suggested that for simple craters the shallow water regime applies for $h/L < 3$–4; however, significant rim modification did occur in simulations with $h/L > 1$, and only the large-scale morphology of the crater was similar for $1 < h/L < 3$–4. However, other studies demonstrate that if weak sediments lie beneath the water column, morphological features indicative of strong water resurge can occur at smaller h/L ratios (e.g., Mjolnir, $h/L = 0.1$–0.5 [*Shuvalov*, 2002]; Chesapeake Bay, $h/L \approx 0.2$ [*Collins and Wünnemann*, 2005]; and Lockne Crater, $h/L \approx 1$ [*Lindström et al.*, 2005]). For example, *Collins and Wünnemann* [2005] and *Kenkmann et al.* [2009] proposed that the resurge flow at the 85 km diameter Chesapeake Bay crater significantly affected the morphology of the final crater structure. According to their simulations, water-saturated sediments underlying an approximately 500 m thick water layer were washed into the inner crater cavity because of the strong water flow and because of extremely weak strength properties of the sediments (Figure 9). The resulting crater morphology at Chesapeake Bay is characterized by a completely buried inner crater with resurge deposits (the so-called Exmore breccia) and an enlarged outer crater diameter due to the inward transportation of the uppermost sedimentary strata. Similarly, models of the Mjolnir impact by *Shuvalov* [2002] showed that the low strength of shallow sediments led to enhanced slumping and approximately a factor of 2 increase in inward gravitational collapse relative to cratering on land.

4.6.2. Deep Water Impact Regime

[43] In deep water impacts the water layer completely suppresses cratering in the seafloor; no crater-like depression is formed. Laboratory impact experiments and numerical modeling suggest that this occurs for $h/L > 4$–20 [*Gault and Sonett*, 1982; *Shuvalov*, 2002; *Davison and Collins*, 2007; *Baldwin et al.*, 2007]; however, the most recent oceanic impact models, which use impact conditions most typical on Earth and approximate the seafloor target strength most realistically, suggest that no transient crater in the seafloor is formed for $h/L > 5$–6 [*Shuvalov and Trubetskaya*, 2002; *Davison and Collins*, 2007]. Although no crater is formed in the deep water impact regime, some impact-induced modifications of the seafloor may occur as suggested by evidence from the Eltanin impact found by a detailed study of the uppermost pelagic strata [*Gersonde et al.*, 1997]. Parasound mapping of the impact zone revealed a 20–40 m thick zone of chaotically mixed sediments that most probably originate from impact-induced turbulent water currents that were generated by the collapse of the transient crater in the water column. Hydrocode modeling of *Wünnemann and Lange* [2002] of the Eltanin event showed that the uppermost strata was effected by the resurge to a distance of 15 km for an impactor 1 km in diameter and a water depth–projectile diameter ratio of 5, despite no permanent crater forming in the seafloor. Other simulations of the Eltanin impact suggest that the impactor must have been less than 1 km in diameter for the ocean to suppress crater formation on the seafloor [*Shuvalov*, 2002; *Artemieva and Shuvalov*, 2002; *Shuvalov and Trubetskaya*, 2002]. Another feature of deep water impacts is that the temporary removal of the substantial weight of the water column may facilitate uplifting due to isostatic adjustment of seafloor material weakened by shock-induced fracturing [*Davison and Collins*, 2007]. The resulting "crater" morphology is a central high that often rises above the preimpact surface level of the seafloor and an external topographic low carved out by resurge flow. Such a feature is unlike conventional complex terrestrial and extraterrestrial craters (compare final crater morphology in the first and sixth columns in Figure 8).

4.6.3. Intermediate Water Impact Regime

[44] Between the shallow water regime and the deep water regime ($1 < h/L < 6$) the water has a profound effect on the impact cratering process. Transient crater size decreases because of deceleration of the projectile by the water column, and the rapid water resurge affects crater collapse and final crater morphology. Figure 8 shows the transient crater and final crater morphology for different water depths, where the first column depicts the case when no water layer is present. In each case the transient cavity is qualitatively the same: a deep, bowl-shaped depression with a constant depth-to-diameter ratio. As demonstrated in Figure 6, transient crater size decreases approximately linearly with increasing water depth. When analyzing the final crater morphology (Figure 7), besides differences in size, distinct qualitative changes in the crater formation process and the resulting final crater morphology occur if the water depth exceeds ~3 times the impactor diameter of >500 m [*Davison and Collins*, 2007]. In this case the return flow is strong enough to erode the crater rim and to carve out a shallow depression in the seafloor outside the transient crater. Simultaneously, enhanced uplift of the impact-weakened seafloor occurs because of the removal of the overburden of the water layer. Notably, the speed of the return flow affects crater morphology; whereas the flow speed is a function of the water depth. For the same water depth–projectile diameter ratio but smaller projectiles (e.g., $L = 100$ m) the effect is much smaller, and the gross characteristics of the final crater morphology is not substantially altered [*Davison and Collins*, 2007].

[45] The centripetal inflow of water from the adjacent ocean may not be strictly symmetric but may be affected by asymmetries in the crater topography caused by variations in strength of the underlying seafloor or possibly due to oblique impacts [*Lindström et al.*, 2005; *Elbeshausen et al.*,

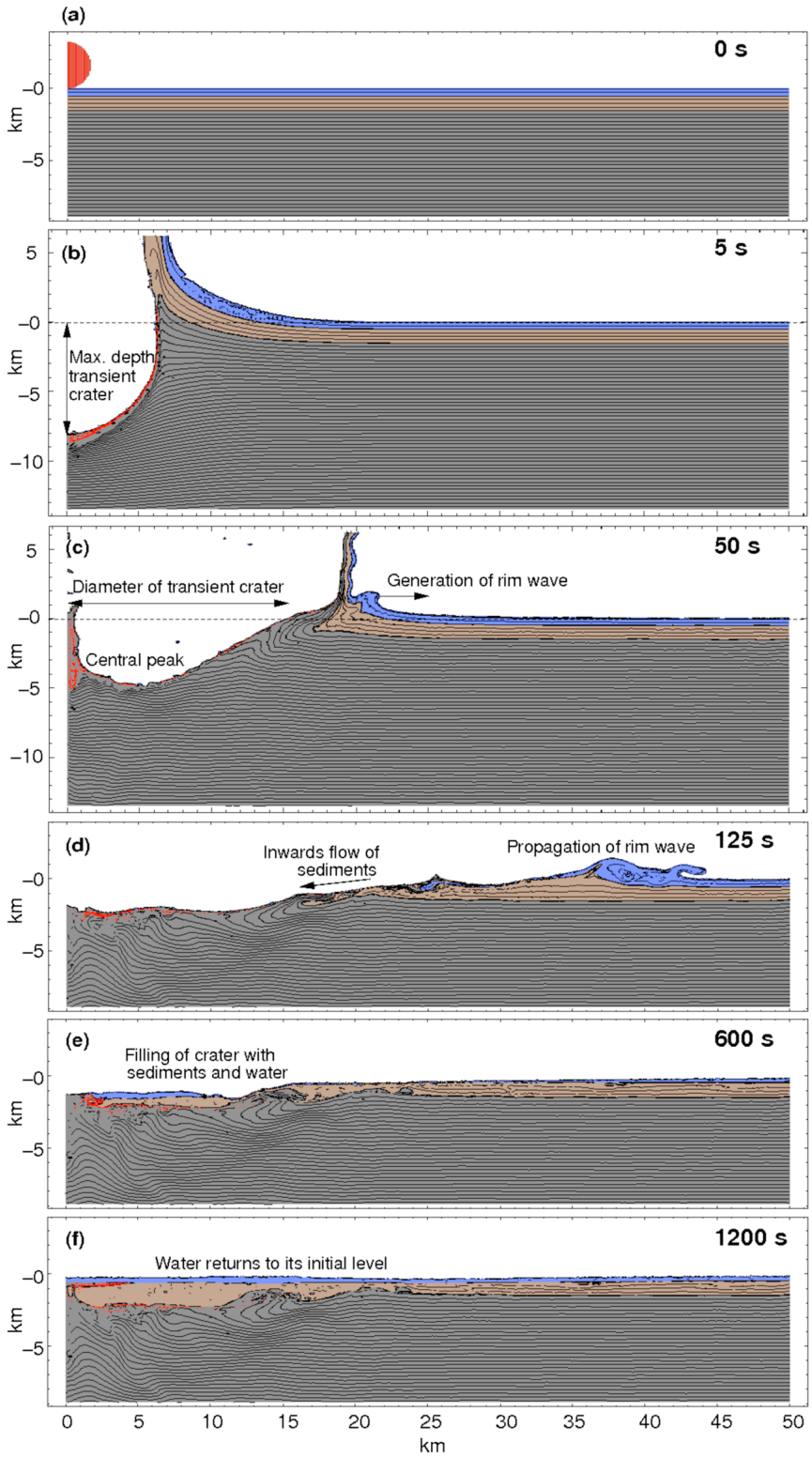

Figure 9. Target deformation from a simulation of the Chesapeake Bay impact using the iSALE hydrocode. The projectile has a density of 2658 km m^{-3} and is 1600 m in diameter. The impact velocity is 16 km s^{-1}. The water is 500 m deep covering a 1 km thick water-saturated, weak sedimentary layer over crystalline basement rocks. (a) The initial setup. (b) After impact a crater is formed that reaches its maximum depth after approximately 5 s. (c) The collapse of the ejecta curtain and crater rim onto the water surface induces a large water wave. (d) Weak sediments and water flow back into the cavity while the rim wave propagates outward. (e and f) The crater is slowly filled by the resurge of weak sediments until the water returns to its initial level.

2009]. The unsteady inflow of water may carve resurge gullies through the crater rim, as proposed at the Lockne crater in Sweden [*Lindström et al.*, 1996; *von Dalwigk and Ormö*, 2001]. Applying a simplified dam break model for the flow over a given crater topography, a 200 m thick initial water column produced an erosive force comparable to the Lake Missoula flood event, the greatest known flood on Earth. For 500 m deep water the stream power is even 1 order of magnitude larger [*Ormö and Miyamoto*, 2002]. The formation of gullies channelizes the resurge flow back into the cavity, leading to an amplification of erosion inside the channels. The extremely complex interaction at the interface between the water and the seafloor was also addressed in full hydrocode models of crater formation and subsequent water return flow. With the help of crater structures that were formed at different water depths (note that the paleo-water depth can be only estimated), the effect of the water layer has been studied by a number of hydrocode models.

[46] The effect of an intermediate water depth (relative to the size of the impactor) was studied by hydrocode modeling of the Lockne crater [*Ormö et al.*, 2002; *Shuvalov et al.*, 2005]. According to this research, crater formation and final crater morphology were distinctly affected by the presence of a water layer. However, in case of the Lockne crater these models do not confirm the proposed formation of resurge gullies but rather suggest deeper water that directly collapses into the crater cavity.

5. IMPACT-INDUCED TSUNAMI HAZARD

[47] Besides the direct local environmental consequences of oceanic impact, large waves are generated that may have destructive consequences for coastal areas hundreds, perhaps even thousands, of kilometers away. These large waves are understood as tsunami waves; however, they differ considerably from waves generated by earthquakes, the most frequent source of tsunamis. Tsunami waves from earthquakes are often hundreds of kilometers long and in the deep ocean only centimeters to decimeters in amplitude. The 2004 Sumatra tsunami, for example, produced an initial tsunami wave measuring more than 5 m [*Titov et al.*, 2005]. It is indisputable that earthquake-generated tsunami represent a significant hazard to coastal megalopolises. The subject of this section is whether impact-generated tsunami waves pose a similar threat to coastal communities.

5.1. Collapse of the Crater in the Water Column and Wave Generation

[48] Experimental work and numerical modeling suggest that the ratio between the water depth h and the projectile diameter L determines the characteristics of oceanic impacts. As discussed in section 4.6, two end-member cases can be distinguished: the DWI ($h/L > 8$), where no crater in the ocean bottom is formed, and the SWI ($h/L < 1$), where crater formation is not affected by the presence of the water layer. In the following we discuss the formation of large waves by impact and how the water depth relative to the projectile size, the h/L ratio, influences the generation mechanism.

[49] Figure 10 shows a snapshot series of a DWI in Figures 10a–10f and a SWI in Figures 10g–10l. Two different wave generation mechanisms can be identified [*Gault and Sonett*, 1982]: (1) wave formation by the collapse of the ejecta curtain and crater rim plunging onto the water surface and (2) wave formation by the collapse of the transient crater. During crater excavation material is ejected and forms an almost vertical standing cone of more or less continuous matter as the direct extension of the uplifted crater rim, the so-called ejecta curtain (Figures 10b and 10h). The ejecta curtain collapses and plunges onto the water surface (Figures 10b, 10c, 10h, and 10i) generating the first wave, the so-called rim wave [*Gault and Sonett*, 1982]. For SWI, the rim wave detaches from the transient cavity and propagates away from the impact site (Figure 10i). In the case of DWI the rim waves decay almost immediately (Figure 10c) and can be neglected in the far field. Gravitational collapse and filling of the transient crater generate the second type of waves. The transient crater fills by centripetal inflow from the adjacent ocean [*Melosh*, 2003]. The water flowing into the cavity generates a central peak (Figures 10c, 10d, 10i, and 10j), whose gravitational collapse results in the formation of the so-called collapse waves (CW) [*Weiss et al.*, 2006]. For most deep water impacts, the timing of the ejecta curtain plunging on the water surface and the filling of transient crater is such that the development of the bidirectional flow dissipates most of the rim wave energy [*Wünnemann et al.*, 2007]. The sequence repeats (oscillations occur in the crater center (Figures 10e and 10k)) until the energy is dissipated and the water layer returns to the preimpact level. Under the assumption of a constant water depth, the waves converge to concentric, radially symmetric shapes independent of the impact angle [*Shuvalov*, 2002].

[50] The superposition of inward and outward directed flow generates a complicated near-field wave pattern. For the inward directed flow, the water depth controls the magnitude of the surge to fill the transient cavity and the height of the central peak of water. Hence, the water depth also affects the characteristics of the generated waves [*Wünnemann et al.*, 2007].

[51] In cases where the diameter of the impactor is much larger than the water depth ($h/L \ll 1$), the crater rim formed on the seafloor may reach above the preimpact sea level, preventing water from directly flowing back into the crater, and no CW can be formed (see section 4.6 [*Bahlburg et al.*, 2010]). Both wave types propagate away from the impact area and may be considered as tsunami waves. The evolution of the wave characteristics as the waves propagate away from the impact area depends mainly on the initial wave steepness, the bathymetry, and other nonlinearities induced by the generation mechanism.

[52] Classical tsunami waves are generated by earthquakes and are known for traveling large distances with the potential to destroy coastal infrastructure in the far field. To explore whether impact-induced waves pose a similar threat, the generation mechanism and resulting wave characteristics of impact-generated waves must be compared to water waves generated by earthquakes. In section 5.2, we relate

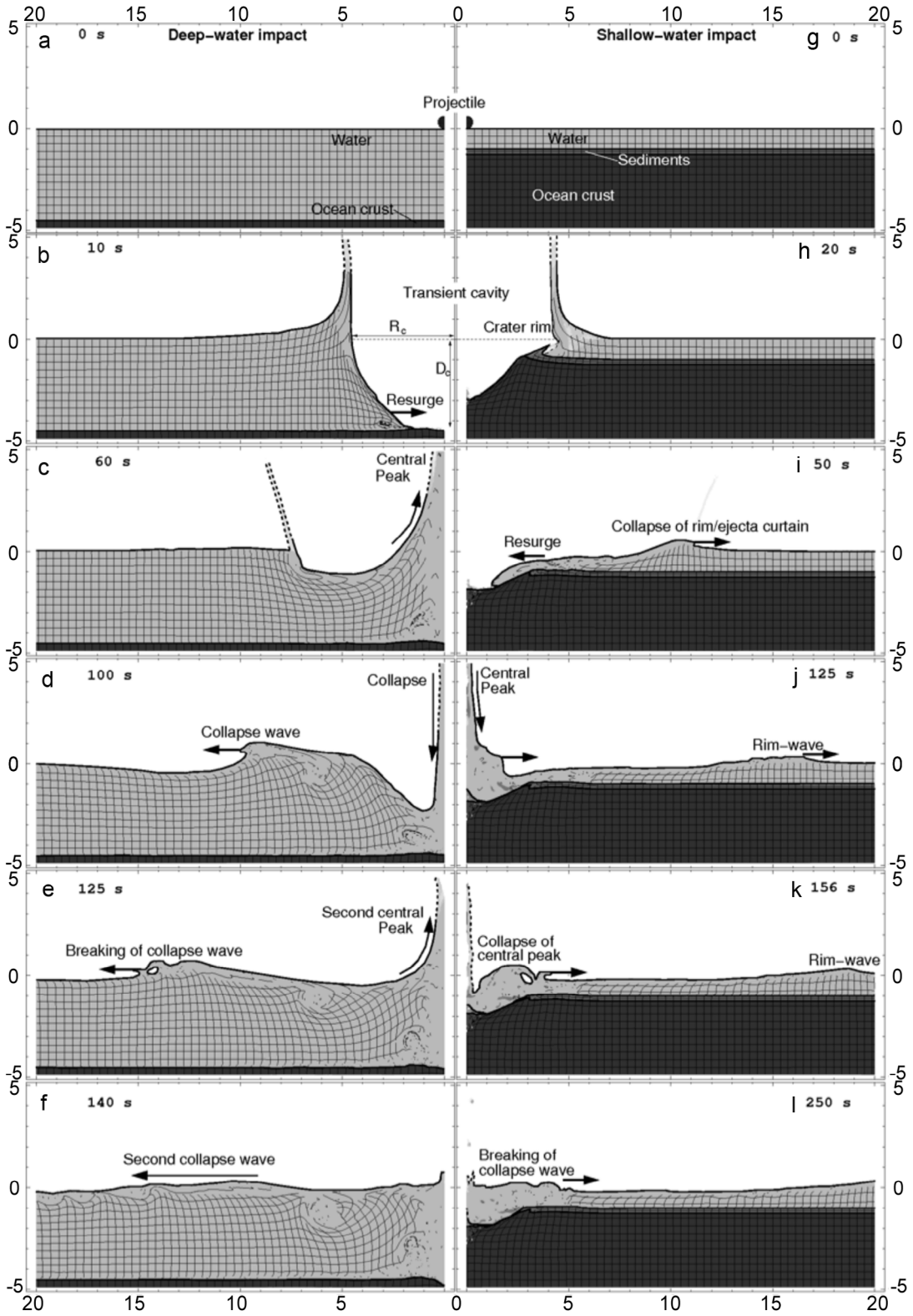

Figure 10. Snapshot series of (left) a deep water and (right) a shallow water impact with $h/L = 4.5$ ($\gamma = L/h = 0.22$) and $h/L = 1.7$ ($\gamma = L/h = 0.6$). Light gray indicates the water column, medium gray indicates a thin layer (250 m) of water-saturated sediments (only present in the SWI), and dark gray indicates the basement. The overlaid grid depicts the deformation. In regions where mixing and turbulent flows occur, no grid is plotted. R_c and D_c mark approximately the radius and depth of the transient crater. Reprinted from *Weiss and Wünnemann* [2007, Figure 9] with kind permission of Springer Science and Business Media.

classical tsunami theory to the characteristics of impact-generated waves.

5.2. Classical Tsunami Theory and Impact-Generated Waves

[53] How do waves generated by impact differ from those generated by more common sources for classical tsunami waves such as earthquakes and landslides? To understand the importance of wave characteristics on wave propagation and how the propagation of waves can be described by an appropriate set of equations, it is necessary to reiterate some principles of fluid dynamics.

[54] The Navier-Stokes equations are derived from Newton's second law of motion and predict fluid flow most appropriately. They contain seemingly all necessary terms to describe the multiscale phenomena that fluid flow exhibits. However, finding an analytical solution to these equations in the full domain of the three-dimensional space as an unsteady problem is difficult, maybe even impossible. Full-scale flow simulations featuring the Navier-Stokes equations would require direct numerical simulations that are computationally very expensive and mathematically challenging because of the multiscale nature of tsunamis [see, e.g., *Gisler*, 2008]. However, the Navier-Stokes equations can be simplified to equations that can be handled in simulations. For example, the assumption that the fluid is inviscid reduces the Navier-Stokes equations to the Euler equations. Further simplifications of the Euler equations, such as the stipulation that the amplitude of tsunami waves and the water depth in which tsunami waves propagate are both small compared to the tsunami's wavelength, result in shallow water equations (SWE). If the water depth is constant, the SWE simplify even further into the wave equation. SWE can be linear and nonlinear, and when derived from the Navier-Stokes equations retaining second-order series expansions of gradients, the resulting equations are called the Boussinesq equations [*Peregrine*, 1967]. Using the linear or nonlinear shallow water equations or the Boussinesq equation, the propagation of tsunami waves can be approximated in a domain of one-dimensional space (along a ray-path) and time or in a domain of two-dimensional space (the water surface) and time.

[55] For the physical simplifications of the linear and nonlinear versions of SWE to be valid, the wavelength has to be on the order of 20 times larger than the water depth. Earthquake-generated waves meet this criterion. The SWE, in general, neglect dispersion because group and phase speed coincide. Only geometrical spreading causes the wave amplitude to decrease. For constant water depth and a circular initial water disturbance meeting the shallow water criteria, the circular wave pattern propagates away from the source area, and the amplitude A decreases as a function of the inverse square root of the distance r: A is proportional to $r^{-1/2}$. For smaller water-depth-to-wavelength ratios, group and phase speed diverge, and the Boussinesq equations need to be applied. For example, the Boussinesq equation derived by *Lynett et al.* [2002] holds to a possible water-depth-to-wavelength ratio where the group speed is almost half the phase speed. With the help of these equations, landslide-generated tsunami waves can be studied [*Lynett et al.*, 2003; *Lynett and Liu*, 2005]. The generation of waves by landslides is fundamentally different to the generation of waves by earthquakes [*Okal and Synolakis*, 2004]. The time scale of an earthquake is short enough compared to the wave period that wave generation can be assumed to be instantaneous. Therefore, the final deformation field of the ocean floor is superposed on the ocean surface as an initial condition. The time scale of landslides is longer; hence, the influence of gravitational equilibrium is significant, and the generation process must be included in the tsunami simulation [*Okal and Synolakis*, 2004]. Landslide-generated waves are larger in amplitude and shorter in wavelength than earthquake-generated waves. Assuming a constant water depth and a circular initial water disturbance but now generating much shorter waves close to a water-depth-to-wavelength ratio of 2, the effect of dispersion needs to be superposed onto geometrical spreading. Wave amplitudes decrease inversely with distance traveled away from the generation area.

[56] As discussed in section 5.1, oceanic impacts generate two distinct wave types: rim waves, which dominate in shallow water impacts, and collapse waves, which dominate in deep water impacts. Rim waves of shallow water impact meet the criterion for shallow water waves, whereas collapse waves do not [*Wünnemann et al.*, 2007]. For a spectrum of wave characteristics, the choice of governing equations (SWE or Boussinesq equations) depends on type of impact. In any case, for distances smaller than 5.3 R_c, in which R_c is the radius of the transient crater, strong wave breaking and plunging does not allow for the use of either shallow water nor Boussinesq equations; simulation of the two-dimensional, vertical model domain is necessary.

5.3. Propagation of Impact-Generated Tsunami Waves

[57] The complexity and duration of the wave generation process in an oceanic impact imply that modeling the resulting wave propagation and predicting the attenuation of wave amplitude with distance are challenging endeavors. Impact wave propagation in a water layer of constant depth has been studied by analogy with underwater explosions, by small-scale impact experiments, and by a range of numerical modeling strategies. Figures 11 and 12 summarize the results of predictions of impact wave attenuation with distance for both shallow water impacts ($h/L < \sim 1$) and deep water impacts ($h/L > 5$). In both Figures 11 and 12 scaled impact tsunami amplitude (height above water level) is plotted against scaled radial distance r/R_w. For deep water impacts wave amplitude is most sensibly scaled by the water cavity radius R_w; for shallow water impacts wave amplitude is most sensibly scaled by water depth h. Perhaps unsurprisingly, the predictions from these studies vary by a factor of 2–3, which has led to differences in estimates of the impact tsunami hazard in the literature.

[58] In many respects, hypervelocity impacts resemble explosions; hence, one approach for estimating impact wave attenuation is to scale the results of underwater nuclear

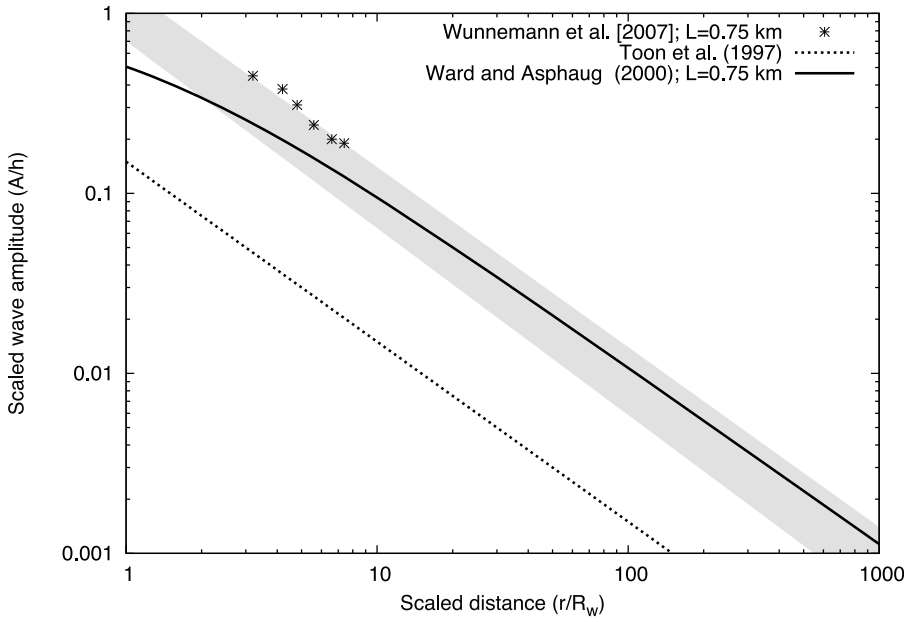

Figure 11. Wave attenuation as a function of distance from point of impact for shallow water impacts ($h/L < \sim 1$) based on hydrocode modeling (stars [*Wünnemann et al.*, 2007]), laboratory experiments (dotted line [*Toon et al.*, 1997]), and theoretical considerations (solid line [*Ward and Asphaug*, 2000]). Wave amplitude A (height above water level) is scaled by water depth h, and distance r is scaled by the radius of the water cavity R_w. The shaded area indicates the discrepancy between different studies summarized in the scaling equations (7)–(9).

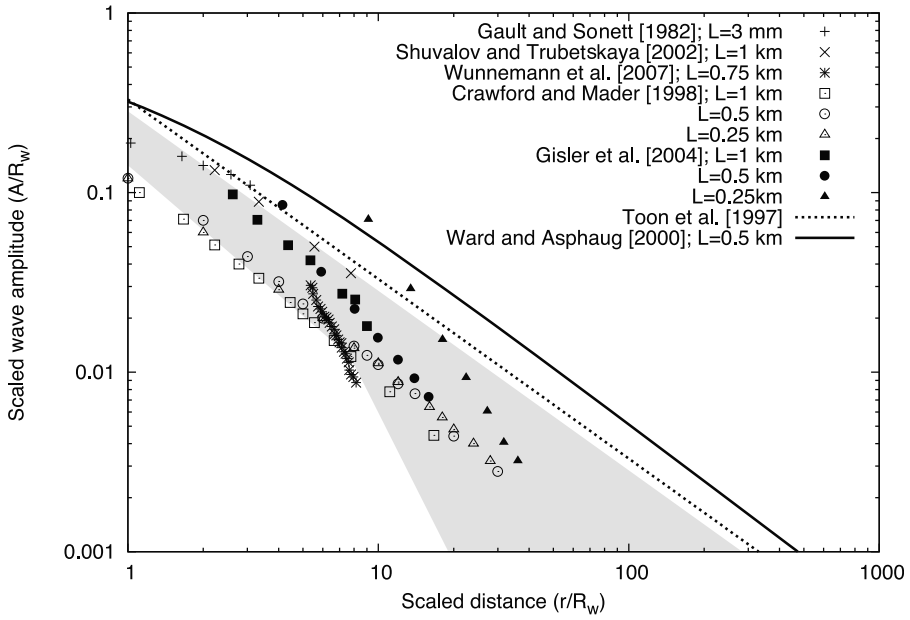

Figure 12. Wave attenuation as a function of distance from point of impact for deep water impacts ($h/L > 5$). Wave amplitude A (height above water level) and distance r are scaled by the radius of the water cavity R_w. Lines and symbols indicate results by different authors using different methods to study wave attenuation: *Crawford and Mader* [1998] (CTH hydrocode and ZUNI propagation model), *Shuvalov and Trubetskaya* [2002] (SOVA hydrocode model), *Gisler et al.* [2003] (SAGE hydrocode model), *Wünnemann et al.* [2007] (iSALE hydrocode model), *Gault and Sonett* [1982] (laboratory experiments), *Toon et al.* [1997] (laboratory experiments and theoretical considerations), and *Ward and Asphaug* [2000] (theoretical considerations). Note that water depth h and impact velocity may vary between different models. Shaded area indicates the large discrepancy between different modeling results, experimental studies, and theoretical considerations. The different decay behavior ranges between r^{-1} (solid and dotted lines) and r^{-3} (black stars) and is summarized in equations (7)–(9).

explosion data to the appropriate impact scale. This strategy was adopted by *Hills and Goda* [1993] and *Hills et al.* [1994], who used nuclear explosion data presented by *Glasstone and Dolan* [1977] to estimate wave amplitudes in deep and shallow water for impacts of energy E ($=0.5mU^2$) in kt TNT equivalent. For impacts into deep water (where the energy-scaled water depth $h/E^{1/4} > 122$ m),

$$A_{tc}(r) = 9000\ (E)^{0.5}\left(\frac{1}{r}\right), \tag{5a}$$

and for shallow water impacts (where $h/E^{1/4} < 26$ m),

$$A_{tc}(r) = 45\ (E)^{0.25}\left(\frac{h}{r}\right). \tag{5b}$$

In these equations A_{tc} is the wave amplitude (trough to crest), h is the water depth, r is the distance from the impact point, and all distances are in meters. Note that neither of these equations are strictly valid for intermediate water depths, where $26 < h/E^{1/4} < 122$ m. These equations demonstrate the important observations that (1) in shallow water impacts/explosions much less energy is partitioned into excavating the water cavity than in a deep water impact/explosion and (2) in deep water (where the crater depth is much smaller than the water depth) the wave height is independent of the water depth, whereas in shallow water wave height is proportional to the water depth.

[59] An alternative strategy for predicting impact wave attenuation is to scale the results of small-scale laboratory impact experiments. *Toon et al.* [1997] used results and scaling arguments from impact experiments into water-covered targets by *Gault and Sonett* [1982] to establish a simple wave amplitude attenuation scaling law for deep water ($h/E^{1/4} > 270$ m),

$$A_{tc}(r) = 9700(E)^{0.5}\left(\frac{1}{r}\right), \tag{6a}$$

and for shallow water ($h/E^{1/4} < 270$ m),

$$A_{tc}(r) = 36(E)^{0.25}\left(\frac{h}{r}\right). \tag{6b}$$

As with equations (5a) and (5b) all distances are in meters, and the impact energy E is in kilotons.

[60] Implicit in both of the above scaling laws is a maximum wave amplitude at the rim of the transient crater in the water. According to crater scaling of *Gault and Sonett* [1982], the transient crater radius (in meters) in the water $R_w = 121(E)^{0.25}$. Hence, for deep water impacts the maximum wave amplitude (trough to crest) predicted by these scaling laws is 0.61–0.66 R_w. (If the wave amplitude A is defined as height above water level (as in Figures 11 and 12), the maximum amplitude at the rim is $A = A_{tc}/2 =$ 0.3–0.33 $R_{w.}$. Note that as the scaling laws of *Toon et al.* [1997] and *Hills and Goda* [1993] are quite similar we include only the former in Figures 11 and 12.) This is at the upper limit of wave heights suggested by numerical modeling (below and Figure 11), but it is reasonable. Similarly, in shallow water impacts large-amplitude waves are implicitly limited by the depth of the water so that the maximum wave amplitude is not larger than 0.3–0.4h, which is in considerable disagreement with numerical models of shallow water impacts (Figure 12). Thus, equations (5b) and (6b) are likely not valid for impacts where a large crater is formed in the seafloor, as discussed by *Shuvalov and Trubetskaya* [2002].

[61] Three different numerical model approaches have been used to study the propagation of impact-generated tsunami: (1) a hybrid method in which the impact and wave generation are simulated with one code and the results of this are used to initialize a separate calculation of the far-field wave propagation with another code [e.g., *Crawford and Mader*, 1998; *Weiss et al.*, 2006; *Glimsdal et al.*, 2007]; (2) a single-code method, where impact, wave generation, and wave propagation are simulated in one calculation with an extended domain to allow for some wave propagation [e.g., *Gisler et al.*, 2003, 2004; *Wünnemann et al.*, 2007]; and (3) an analytical method, in which an impact-like initial wave signal is propagated forward according to linear wave theory [e.g., *Ward and Asphaug*, 2000, 2003; *Ward*, 2002].

[62] The hybrid method was first adopted by *Crawford and Mader* [1998]. They used the CTH code to compute the formation of impact-generated water cavities in deep water (h/L = 5–20) and the ZUNI code to simulate the collapse of the cavity and the propagation of waves for a distance of 150 km. The ZUNI code numerically solves the incompressible Navier-Stokes equations [*Mader*, 1988] and hence is more suited to simulating subsonic flow. The timing of the transition between CTH and ZUNI was based on the physical reasoning that shock wave propagation is diminished and can be neglected from the time of transient crater formation. However, the ZUNI wave propagation simulation was initialized with a simplified transient crater geometry in which the uplifted rim was neglected and with zero velocity in the water mass. Hence, rim wave propagation was not modeled; only the radial decay of the collapse wave amplitude was measured. Results from these simulations (for water cavities 2.5, 5, and 10 km radius in a 5 km deep ocean) are presented in Figure 12. Interestingly, according to these results attenuation of tsunami wave amplitude is almost independent of h/L when scaled by the water cavity dimension. Maximum wave amplitudes (here defined as height above ocean level) at the transient crater rim were in the range 0.09–0.12 R_w, and amplitudes were observed to decay in proportion to r^{-1}. For example, an asteroid (density of 3320 km m^{-3}) of 500 m in diameter with an impact velocity of 20 km s^{-1} produced a 5 km radius water cavity, with a 600 m high wave at the cavity rim that decayed to 14 m in height by 150 km radius.

[63] A similar approach was employed by *Weiss et al.* [2006], who simulated the entire impact tsunami process with a hybrid technique consisting of impact modeling, wave propagation, and modeling of the nearshore evolution (Figure 13). The code iSALE was employed for the impact modeling. The evolution of the water column was computed

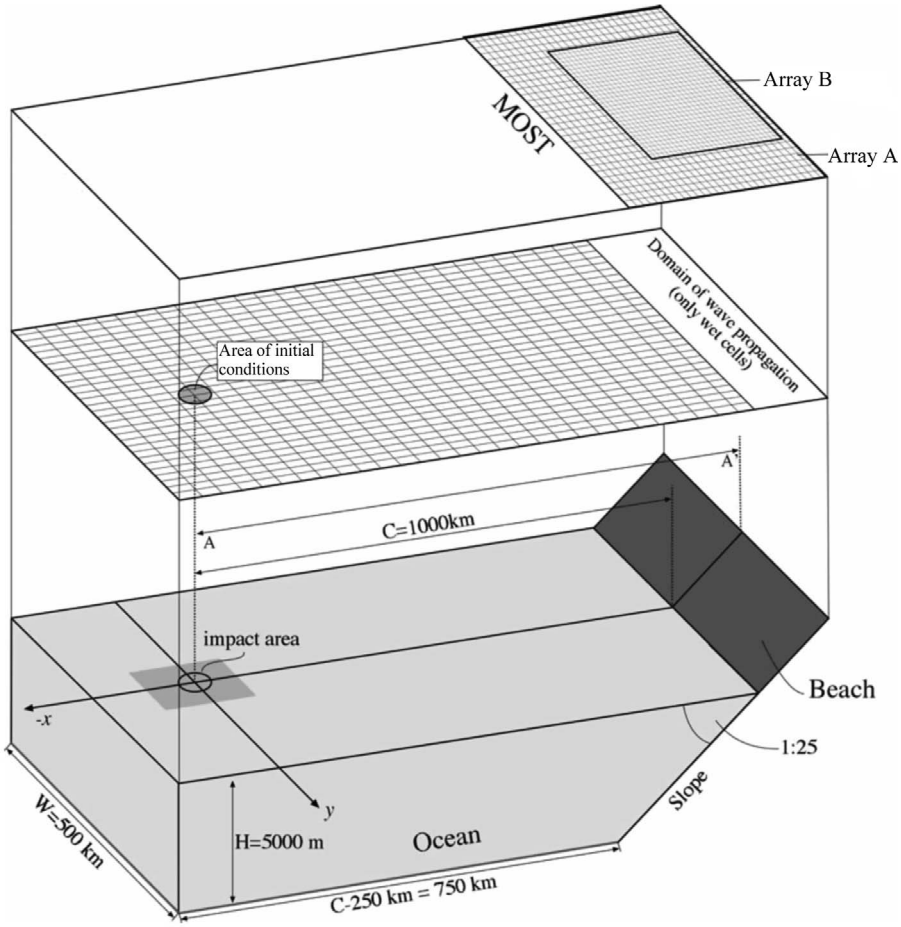

Figure 13. Experimental setup of *Weiss et al.* [2006]. (bottom) An example bathymetry with C as the distance between the point of impact and the shoreline. Along the section A-A′, the wave elevation is recorded by gauge points (see Figure 12). The impact area is highlighted by the circle. (middle) The domain of the wave propagation, covering only the wet part of the example bathymetry. (top) The arrangement of arrays for the wave propagation as well as arrays A and B used in MOST. Reprinted from *Weiss et al.* [2006, Figure 6], copyright 2006, with permission from John Wiley.

for vertical impact up to the point where wave behavior was simple enough to define an initial wave pattern for the wave propagation. A Boussinesq-type wave code was employed to compute the wave propagation to the nearshore area, where the MOST model computed the wave evolution including inundation. In the deep water (h/L = 6.25) example presented by *Weiss et al.* [2006], a maximum wave height (above ocean level) of approximately 0.1–0.2 R_w was observed between radial distances of 1–2 R_w, and wave amplitude attenuation was proportional to r^{-1}. In the given example the wave attenuation 1000 km away from the impact area resulted in a runup of about 10 m, attenuation 2000 km away from the impact area resulted in a runup of about 5 m, and attenuation 3000 km away from the impact area resulted in a runup of about 2 m (Figure 14). These three runup values are on the order of what was measured in the aftermath of the 2004 Sumatra tsunami in the Indian Ocean [*Synolakis and Kong*, 2006].

[64] The tsunami waves generated during the shallow water Molnjir impact event in the Barents Sea, 142 Ma, were modeled with SOVA and hydrodynamic techniques by *Glimsdal et al.* [2007]. SOVA [*Shuvalov et al.*, 2002; *Shuvalov*, 1999] was employed to simulate the impact, but for the wave evolution several techniques were compared. An undular bore was formed in the early stage of wave propagation. Such waves are highly nonlinear and require high-order Boussinesq approaches to simulate. *Glimsdal et al.* [2007] argue that for the given available computational resources, a reliable and complete modeling with such approaches cannot be computed in the required resolution because of the physical processes acting on the generated waves. However, techniques borrowed from optics lead to reasonable results [*Glimsdal et al.*, 2007].

[65] The approaches that employ only one model are extremely useful for studying early wave dynamics and early wave propagation. *Shuvalov and Trubetskaya* [2002] measured wave attenuation in a SOVA simulation of the Eltanin impact, in which a 1 km diameter asteroid impacted water 4 km deep at 20 km s^{-1}, forming an ~10 km radius water cavity. In this case, which is on the threshold of being a deep water impact (h/L = 4), rim wave amplitude decayed as approximately r^{-1} over the first 70 km, from a maximum

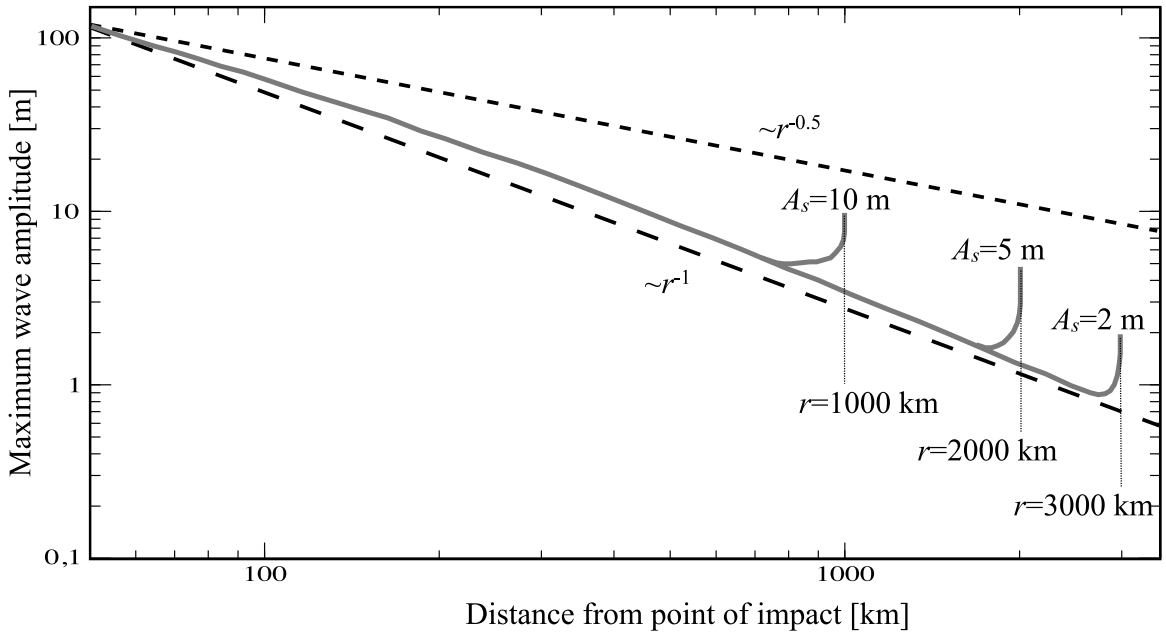

Figure 14. A log-log plot of the maximum wave amplitude versus distance to the impact center (solid lines). The dotted line shows the damping of the wave elevation obeying a function proportional to $r^{-0.5}$; the dashed line resembles damping proportional to r^{-1}. A_{bt} is the wave height at the beach toe, and A_s is the runup height at different distances r to the point of impact: A_s = 10 m for r = 1000 km, A_s = 5 m for r = 2000 km, and A_s = 2 m for r = 3000 m. Modified from *Weiss et al.* [2006, Figure 7b], copyright 2006, with permission from John Wiley.

height (above ocean level) of 1200 m at 20 km radius (i.e., 0.12 R_w at 2 R_w). In two- and three-dimensional simulations, *Gisler et al.* [2004] showed that for various asteroid types and diameters the proximal wave damping in deep water ($5 < h/L < 20$) impacts is a function of r^{-q}, where q varies between 1.3 and 2.25 (Figure 12), depending on the ratio h/L. No distinction was made between rim and collapse waves. Maximum wave amplitudes at the transient crater rim were not reported but are consistent with the results of other modeling studies, as can be seen from Figure 12. In a similar study, *Wünnemann et al.* [2007] found that for constant impact energy, the attenuation factor q in r^{-q} (Figure 15) increases with increasing h/L and depends on the type of wave (rim versus collapse). The collapse waves, which only occur in intermediate/deep water impacts, undergo stronger decrease in amplitude (q = 2.7–3.32) than the rim waves (q = 0.8–1.3), which are only prominent in shallow water impacts. Again, maximum wave amplitudes at the water cavity rim (R_w) were not reported in this work but did not exceed 0.1–0.15 R_w for either the collapse or rim wave. Furthermore, for deep water impacts wave attenuation was well behaved only outside radial distances of about 5 R_w, at which point a maximum wave height (above water level) of 0.06 times the smaller of the water depth h and the transient crater diameter in the water (2 R_w) was observed. Wave amplitude variation was found to be very complex inside a radius of ~5 R_w because of wave breaking.

[66] The strong attenuation of collapse waves at proximal distances observed by *Gisler et al.* [2004] and *Wünnemann et al.* [2007] is in stark contrast with the canonical r^{-1} decay observed in earlier hybrid model approaches (and predicted by scaling laws based on experimental and explosion data). Evidently, more work is required to carefully verify the results of these studies and explain the discrepancies between them; however, taken at face value, they suggest that if a separate model is used to simulate distal wave propagation, either it must be capable of simulating wave breaking itself or, if not, the impact-generated wave signal used to initialize the model must be captured several crater radii from the impact site where the waves are well behaved.

[67] *Wünnemann et al.* [2007] ascribe the different behavior of collapse and rim waves to different water dynamics indicated, for example, by different profiles of the horizontal water velocity with depth. For rim waves, the horizontal velocity of the water shows no change with depth outside the boundary layer (Figure 16b); for collapse waves, on the other hand, the horizontal velocity of the water decreases dramatically with depth (Figure 16a). According to the definition of different waves, the rim waves of shallow water impacts are also shallow water waves, and the collapse waves of deep water impacts are deep water waves.

[68] Analytical wave theory with impact-like initial conditions was explored by *Ward and Asphaug* [2000]. *Ward and Asphaug* [2000] focused on deep water impacts because they are much more frequent, and the authors argue that the shape of the transient crater in the water can be approximated by a parabolic function for distances smaller than the crater radius (crater size was estimated using scaling laws [*Schmidt and Housen*, 1987]; see section 4.2).

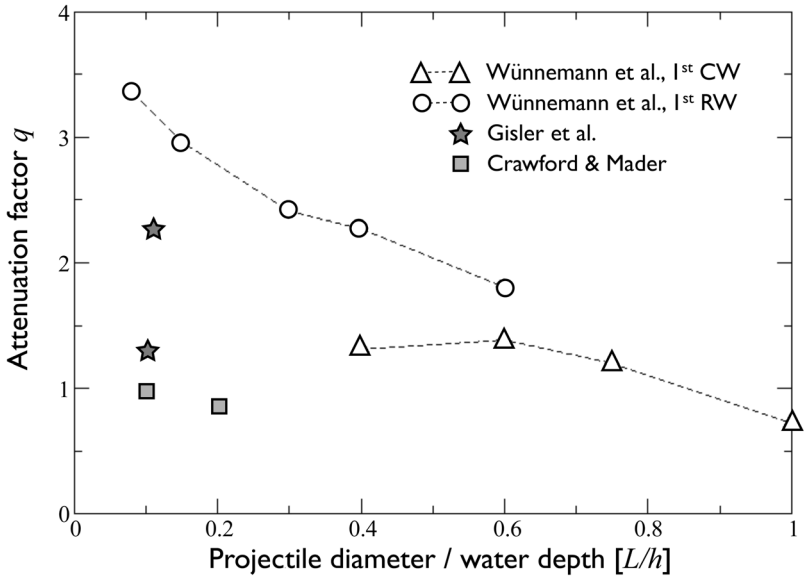

Figure 15. Attenuation factor q of the first collapse wave (CW, circles) and the rim wave (RW, triangles) as a function of L/h ratio for $r > 5.3 \times R_c$ [*Wünnemann et al.*, 2007]. Stars and squares mark the attenuation factors found by *Gisler et al.* [2003] and *Crawford and Mader* [1998].

With this type of simplified initial condition, the impactor's kinetic energy must completely dissipate within the water. Moreover, the simplified initial conditions imply a maximum wave amplitude at R_w approximately equal to 0.33–0.4 R_w for deep water impacts. As shown in Figure 12, which plots the results of *Ward and Asphaug* [2000] for $h/L = 10$, this is somewhat larger than data from numerical models. Although not the focus of their study, the results of Ward and Asphaug can be applied with caution to shallow water impacts, where the wave height is limited by the depth of the water. Figure 11 shows that the Ward and Asphaug model is in reasonable agreement with the few numerical model results of shallow water impacts available.

[69] The wave evolution model used by *Ward and Asphaug* [2000] is based on analytical solutions of Euler's equations with an integral approach. It therefore has the advantage of being quick to compute, making it particularly useful for probabilistic hazard assessment. The approach does not assume the shallow water wave theory; therefore, the wave speed is a function of the wave period. The

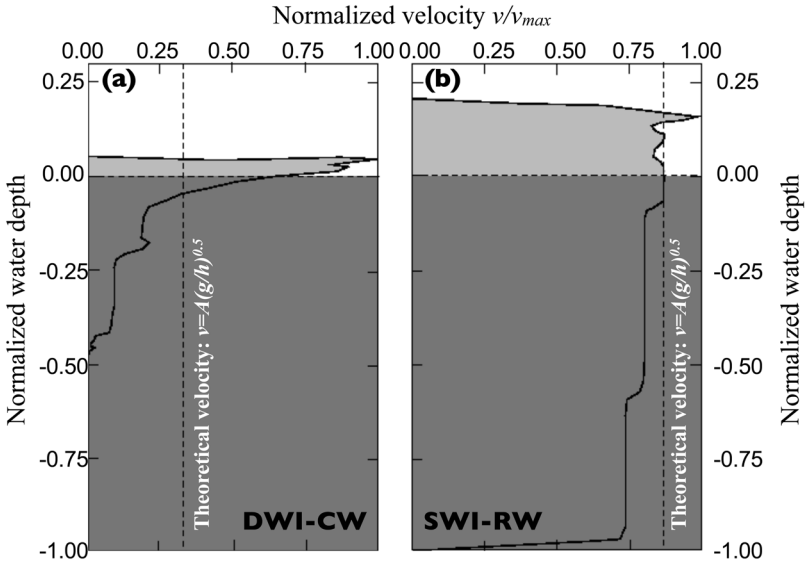

Figure 16. Vertical profile through the water column of the radial velocity component (a) for the CW ($r = 19.6$ km and $t = 300$ s) at a DWI ($L/h = \gamma = 0.15$) and (b) for the RW ($r = 38$ km, $t = 300$ s) at a SWI. The dashed lines mark the theoretically determined velocity of a shallow water wave. Reprinted from *Wünnemann et al.* [2007, Figure 6], copyright 2007, with permission from John Wiley.

resulting equations for wave attenuation show that the decay rate of the maximum amplitude is proportional to r^{-1} (Figure 14), of which $r^{-0.5}$ comes from geometrical spreading and the additional $r^{-0.5}$ comes from dispersive effects by linear wave theory [*Ward and Asphaug*, 2000]. The runup is not directly computed by *Ward and Asphaug* [2000]. Their computations stop at a critical water depth when nonlinear processes such as wave breaking would occur as these are not considered by their linear approach. The maximum wave elevation at this critical water depth is then combined with impact frequency to carry out probabilistic tsunami hazard calculations. The results obtained by *Ward and Asphaug* [2000] imply that the tsunami waves caused by small impactors can cause widespread devastation in coastal areas. *Ward and Asphaug* [2003] considered a case study of a potential impact of asteroid 1950 DA on 16 March 2880. The likelihood of this impact occurring was estimated to be between 0.0% and 0.3% [*Giorgini et al.*, 2002], or more precisely, with the help of random background probability and assuming a recurrence interval of 375,000 years, the likelihood is 0.23% [*Ward*, 2002]. Ward and Asphaug found a representative impact site at 35°N and 70°W in the Atlantic Ocean about 600 km offshore of the U.S. east coast. They projected that 40–70 m large waves would approach the east coast and that 10–20 m waves would arrive at the European and African coasts.

[70] The discrepancy in maximum wave amplitude and wave attenuation between different studies highlighted in Figures 11 and 12 is perhaps symptomatic of the very different approaches used to investigate the problem. Evidently, more numerical models and experiments are required to clarify the reasons for the discrepancy and provide some consensus, particularly for shallow water impacts. It is likely that the discrepancies between the different hybrid numerical model results for deep water impacts are a consequence of the different methods used to initialize the wave propagation model. Thus, an interesting problem for future research is to find an optimal strategy for transferring the wave signal generated by a numerical impact model into a wave propagation model. Given the efficiency advantage of an analytical approach, particularly for probabilistic hazard assessment, another fruitful avenue for future research would be to repeat the method outlined by *Ward and Asphaug* [2000] using more realistic initial conditions for deep water impacts.

[71] For the present time, the analysis presented here suggests that a reasonable estimate of impact tsunami height as a function of distance from impact in water of constant depth is given by

$$A(r) = \min(0.28\ R_w, h)\left(\frac{R_w}{r}\right), \tag{7}$$

where the water cavity radius R_w must be computed from the most appropriate crater scaling law and the maximum wave height (above water level) at the cavity rim is ~0.28 R_w. This upper bound is appropriate for shallow and deep water impacts alike.

[72] A sensible lower bound estimate can also be defined as

$$A(r) = \min\{A_r(r),\ A_c(r)\}, \tag{8}$$

where A_r and A_c are the amplitudes of the rim wave and collapse wave, respectively, given as

$$A_r(r) = \min(0.14\ R_w, h)\left(\frac{R_w}{r}\right)^{q_r} \tag{9a}$$

$$A_c(r) = 0.06 \min(R_w/3, h)\left(\frac{5R_w}{r}\right)^{q_c}. \tag{9b}$$

In this case, for the rim wave a more conservative maximum wave height of 0.14 R_w at the cavity rim is assumed, which is consistent with estimates for transient crater rim height that assume volume conservation [*Collins et al.*, 2005], and the attenuation factors q_r and q_c are given by

$$q_r = \min\left(1.2, 0.5 + 2e^{-1.75L/h}\right) \tag{10a}$$

$$q_c = 3e^{-0.8L/h} \tag{10b}$$

on the basis of the results of *Wünnemann et al.* [2007] and the fact that in the shallow water limit $q_r = 0.5$. Note also that as collapse waves are not generated in shallow water impacts, equation (9b) is only valid for $h/L < 2$. The ranges defined by these upper and lower bounds are shown in gray in Figure 12 for $h/L = 10$ and in Figure 11 for $h/L = 1.33$. (These upper and lower bound estimates have been incorporated into the Earth Impact Effects Program (http://impact.ese.ic.ac.uk/ImpactEffects), a Web-based calculator for estimating the environmental consequences of impacts on Earth.)

5.4. Shoaling of Impact-Generated Waves

[73] As impact-generated tsunami waves approach a coastline and the water depth shallows, conservation of energy, momentum, and mass result in an increase in wave amplitude, a process known as shoaling, eventually leading to wave breaking. For very large amplitude waves, shoaling may also occur in the open ocean if the water depth shallows abruptly, such as at a continental shelf. This effect is known as the "Van Dorn effect," named after the author of a report on explosion-generated waves [*van Dorn and Le Mehaute*, 1968]. *Melosh* [2003] argued that this effect implies that tsunami waves generated by impact in the deep ocean likely dissipate their energy on the continental shelf. Breaking of these waves dissipates the wave energy effectively so that only a small fraction of the initial wave energy arrives at the shoreline [*Melosh*, 2003]. *Korycansky and Lynett* [2005, 2007] investigated in detail the evolution of large water waves as they approach a shelf and propagate on it. Their computations are two-dimensional, with one dimension for space and one for time. The bathymetries used correspond to piecewise linear sections of simplified Gulf of Mexico and Pacific Ocean margins. The model suite pCOULWAVE

[*Lynett et al.*, 2002] was applied for the wave propagation, which is a Boussinesq-type long-wave code. This code is fully capable of taking the nonlinear processes into account that would result in the Van Dorn effect: breaking of the waves. Results show that large waves diminish while propagating over the continental shelf [*Korycansky and Lynett*, 2005, 2007], which supports the existence of the Van Dorn effect. However, they did not input waves that were the outcome of impact cratering calculations; rather, they applied linear approximations, such as those presented by *Ward and Asphaug* [2000], and scaling. Nonetheless, Korycansky and Lynett's results directly challenge results by *Ward and Asphaug* [2000].

[74] On the other hand, the Van Dorn effect requires steep and large waves at the shelf edge if waves are to break. Not all impact-generated waves will be steep enough or large enough to break at the shelf edge. For example, waves with an amplitude of 100 m near the impact area would reduce to 4.61 m after 750 km of propagation, 1.54 m after 1750 km of propagation, and 0.8 m after 2750 km of propagation (Figure 14 [*Weiss et al.*, 2006]). Therefore, it is not yet clear whether the Van Dorn effect is always important and whether large tsunami-like waves generated by oceanic impacts pose a substantial hazard.

6. SUMMARY AND DISCUSSION

[75] The impact of a relatively small asteroid (50–200 m) into a marine environment is statistically the most likely scenario for a future meteorite impact event [*Hills et al.*, 1994; *Ward and Asphaug*, 2000] because of the fact that oceans cover approximately 70% of Earth's surface. If the fraction of Earth's surface covered by landmasses has not changed significantly in the past, most impact events in Earth history occurred in the ocean. Besides important field studies that have revealed specific morphological features of submarine impact structures, laboratory hypervelocity impact experiments into layered targets and numerical modeling have contributed greatly to our current understanding of the specific processes accompanying the strike of a meteorite into an ocean. We discussed a number of essential points that distinguish impacts in marine environment from those on terrestrial continental targets and extraterrestrial surfaces:

[76] 1. First and foremost, the water layer changes the coupling of the impactor's kinetic energy to the seafloor. The thicker the water layer, the smaller the fraction of the impactor's kinetic energy that is transferred to the seafloor and the smaller the crater that is excavated. Besides water depth, impact velocity and, in particular, the strength properties of the benthic strata significantly affect whether a crater is formed in the seafloor or not. Synthesizing experimental and numerical model results for the most realistic and likely initial conditions, the critical water depth required to completely suppress cratering in the seafloor is approximately 6–8 times the projectile diameter for a stony asteroid. The critical water depth will be somewhat smaller for cometary impacts and somewhat larger for iron asteroid impacts. Despite some quantitative uncertainty in the decelerating effect of the water layer on the projectile, this part of the oceanic impact process is probably best understood.

[77] 2. Strong water currents along the seafloor due to the collapse of the transient crater in the water column significantly modify the morphology of oceanic impact craters. Processes unique to submarine crater formation are incoherent, chaotic mixing of the upper most benthic strata; modification of the crater rim ranging from formation of resurge gullies to complete erosion of the crater rim; and more extreme modification of the seafloor such as enhancement of gravitationally driven collapse of the crater in the seafloor (due to the temporary removal of the overburden of the water layer). The modification of crater morphology due to the water column strongly depends on the strength properties of the benthic strata and water depth. Neither is usually well known for terrestrial marine impact craters and can be estimated only by means of other observations indicative of water depth and turbulence of the depositional regime. The relationship between impact energy, water depth, and deformation at the ocean bottom is not very well understood, in particular, for impact events too small to form craters in the ocean bottom. Better quantification of the impact-induced imprint in the ocean bottom based on numerical modeling and observations at known impact sites would help to develop criteria for the search of impact structures in the ocean.

[78] 3. Uplift of the water cavity rim, together with collapse of the ejecta curtain onto the water surface, and the collapse of the transient crater in the water column generate two different types of water waves: so-called rim waves and collapse waves. Analyses of wave characteristics show that both wave types have little in common with classical tsunami waves generated by earthquakes. Rim waves occur only in shallow water and are more similar to landslide tsunami waves than earthquake tsunami waves. Collapse waves occur primarily in deep water and are characterized by a large wave amplitude and short wavelength. Close to the point of impact the waves are nonlinear and undergo wave breaking, resulting in rapid attenuation of the wave amplitude. Farther from the impact site such waves may disperse into longer, smaller-amplitude waves that attenuate less rapidly; hence, it remains possible that impact tsunami waves may threaten coastal areas at large distances. However, as current models, laboratory experiments, and theoretical considerations show large discrepancies in their predictions of the attenuation of impact-induced waves, the hazard of impact-generated tsunamis is still an open question.

[79] Although substantial progress has been made in the last decades by the aid of numerical modeling, our quantitative understanding of oceanic impacts remains incomplete. For the reconstruction of the Earth's impact record, which is key to assessing the frequency of collision events, it is of crucial importance to include the ocean crust as it is the largest fraction of Earth's surface that is exposed to the impact flux. We discussed in detail the various natural

reasons for the apparent paucity of impact structures in the ocean; however, despite these arguments it is beyond debate that many undiscovered impact structures should exist in the ocean crust. *Davison and Collins* [2007] estimate that approximately 100–200 craters >10 km in diameter should exist on a 100 Ma oceanic crust (assuming the present ratio between landmasses and oceans) and that approximately 150–600 events were too small to form craters but may have caused specific resurge features in the weak sediments on the seabed. However, it is unclear what such resurge features might look like. A combined approach of observational, experimental, and numerical modeling work is required to fully understand the nature of these events and develop a catalog of specific signatures of oceanic impact structures. What exactly do we have to look for to detect oceanic impact structures hidden in the stratigraphic record of the ocean basins in order to complete the Earth's impact record?

[80] In addition to the direct search for suspicious structures on the ocean bottom, paleotsunami deposits may also serve as evidence for an oceanic impact event. The main problem here is how to distinguish the tsunami deposits caused by impact-generated waves from those that are the result of large earthquakes, volcanic eruptions, or landslides. The unique character of impact-generated waves may provide a means to identify such deposits. More research efforts are required to further our knowledge of the characteristics of impact tsunami waves and how to recognize related tsunami deposits. The Eltanin event is a possible source of important evidence if it can be related to specific features in the stratigraphic record along the surrounding coast lines. Additionally, numerical modeling can contribute by predicting wave amplitudes, runup heights, and inundation distances along certain areas of the coastline.

[81] If humanity is unfortunate enough to suffer the consequences of a large impact, it will be too late to understand the threat by observation. Hence, we have to rely on numerical model predictions to evaluate the hazard of a cosmic body striking the ocean. As discussed above there is still no accepted predictive, quantitative model of generation, propagation, shoaling, and runup of impact-generated tsunami waves. The main problem here is that different processes happen on very different spatiotemporal scales which are best modeled by different approaches. Work to date has shown that perhaps the best strategy for future work is to combine different numerical models of (1) wave generation by impact (hydrocode modeling), (2) propagation of nonlinear waves in the near field (Boussinesq models), (3) wave propagation models in the far field (possibly linear wave propagation models are applicable), and (4) specific models for shoaling and runup. The coupling of models has to be done with great care, and one has to make sure that specific wave characteristic are not eliminated or generated artificially when passing wave signals from one model into another. A rigorously tested chain of models describing the whole process beginning with the wave generation, ending with the inundation, and taking bathymetry in the ocean and the shape of the coastline into account is essential for a complete impact tsunami hazard assessment and an exciting challenge for future research.

[82] **ACKNOWLEDGMENTS.** This work was funded by DFG grant WU 355/5-2 and NERC grant NE/B501871/1.

[83] The Editor for this manuscript was Pete Riley. He thanks two reviewers, Donald Korycansky and Fabio Florindo.

REFERENCES

Anderson, C. E., Jr. (1987), An overview of the theory of hydrocodes, *Int. J. Impact Eng.*, *5*, 33–59, doi:10.1016/0734-743X(87)90029-7.

Artemieva, N. A., and V. V. Shuvalov (2001), Motion of a fragmented meteoroid through the planetary atmosphere, *J. Geophys. Res.*, *106*, 3297–3309, doi:10.1029/2000JE001264.

Artemieva, N. A., and V. V. Shuvalov (2002), Shock metamorphism on the ocean floor (numerical simulations), *Deep Sea Res., Part II*, *49*, 959–968, doi:10.1016/S0967-0645(01)00136-9.

Bahlburg, H., R. Weiss, and K. Wünnemann (2010), Low energy sedimentary infill of the Chicxulub crater during the impact to post-impact transition, *Earth Planet. Sci. Lett.*, *295*, 170–176, doi:10.1016/j.epsl.2010.03.037.

Baldwin, E. (2008), Investigation of impact crater processes using experimental and numerical techniques, Ph.D. thesis, Univ. Coll. London, London.

Baldwin, E. C., D. J. Milner, M. J. Burchell, and I. A. Crawford (2007), Laboratory impacts into dry and wet sandstone with and without an overlying water layer: Implications for scaling laws and projectile survivability, *Meteorit. Planet. Sci.*, *42*, 1905–1914, doi:10.1111/j.1945-5100.2007.tb00549.x.

Benson, D. J. (1992), Computational methods in Lagrangian and Eulerian hydrocodes, *Comput. Methods Appl. Mech. Eng.*, *99*(2–3), 235–394, doi:10.1016/0045-7825(92)90042-I.

Bland, P. A., and N. A. Artemieva (2003), Efficient disruption of small asteroids by Earth's atmosphere, *Nature*, *424*, 288–291, doi:10.1038/nature01757.

Bland, P. A., and N. A. Artemieva (2006), The rate of small impacts on Earth, *Meteorit. Planet. Sci.*, *41*, 607–631, doi:10.1111/j.1945-5100.2006.tb00485.x.

Century Dynamics, Inc. (2003), AUTODYN theory manual, version 4.3, Horsham, U. K.

Chyba, C. F., et al. (1993), The 1908 Tunguska explosion: Atmospheric disruption of a stony asteroid, *Nature*, *361*, 40–44, doi:10.1038/361040a0.

Collins, G. S., and K. Wünnemann (2005), How big was the Chesapeake Bay impact? Insight from numerical modeling, *Geology*, *33*, 925–928, doi:10.1130/G21854.1.

Collins, G. S., H. J. Melosh, and B. A. Ivanov (2004), Modeling damage and deformation in impact simulations, *Meteorit. Planet. Sci.*, *39*, 217–231, doi:10.1111/j.1945-5100.2004.tb00337.x.

Collins, G. S., H. J. Melosh, and R. A. Marucs (2005), Earth Impact Effects Program: A Web-based computer program for calculating the regional environmental consequences of a meteoroid impact on Earth, *Meteorit. Planet. Sci.*, *40*, 817–840, doi:10.1111/j.1945-5100.2005.tb00157.x.

Crawford, D. A., and C. L. Mader (1998), Modeling asteroid impact and tsunami, *Sci. Tsunami Hazards*, *16*, 21–30.

Davison, D., and G. S. Collins (2007), The effect of the oceans on the terrestrial crater size-frequency distribution: Insight from numerical modeling, *Meteorit. Planet. Sci.*, *42*, 1915–1927, doi:10.1111/j.1945-5100.2007.tb00550.x.

Dence, M. R. (1965), The extraterrestrial origin of Canadian craters, *Ann. N. Y. Acad. Sci.*, *123*, 941–969.

Dienes, J. K., and J. M. Walsh (1970), Theory of impact: Some general principles and the method of Eulerian codes, in

High-Velocity Impact Phenomena, edited by R. Kinslow, pp. 45–104, Academic, New York.

Elbeshausen, D., K. Wünnemann, and G. S. Collins (2009), Scaling of oblique impacts in frictional targets: Implications for crater size and formation mechanisms, *Icarus*, *204*, 716–731, doi:10.1016/j.icarus.2009.07.018.

Engel, O. E. (1961), Collisions of liquid drops with liquids, *NBS Tech. Note*, *89*.

Engel, O. E. (1962), Collisions of liquid drops with liquids. II. Crater depths in fluid impacts, *NBS Tech. Rep.*, *WADD-TR-60-475*.

French, B. (1998), *Trace of Catastrophe*, 120 pp., Lunar and Planet. Inst., Houston, Tex.

Gault, D. E. (1978), Experimental impact "craters" formed in water: Gravity scaling realized (abstract), *Eos Trans. AGU*, *59*, 1121.

Gault, D. E., and C. P. Sonett (1982), Laboratory simulation of pelagic asteroid impact: Atmospheric injection, benthic topography, and the surface wave radiation field, in *Geological Implications of Impacts of Large Asteroids and Comets on the Earth*, edited by L. T. Silver and P. H. Schultz, *Spec. Pap. Geol. Soc. Am.*, *190*, 69–92.

Gault, D. E., W. L. Quaide, and V. R. Oberbeck (1968), Impact cratering mechanics and structures, in *Shock Metamorphism of Natural Materials*, edited by B. M. French and N. M. Short, pp. 87–99, Mono Book, Baltimore, Md.

Gersonde, R., et al. (1997), Geological record and reconstruction of the late Pliocene impact of the Eltanin asteroid in the Southern Ocean, *Nature*, *390*, 357–363, doi:10.1038/37044.

Giorgini, J. D., et al. (2002), Asteroid 1950 DA's encounter with Earth in 2880: Physical limits of collision probability prediction, *Science*, *296*, 132–136, doi:10.1126/science.1068191.

Gisler, R. G. (2008), Tsunami simulations, *Annu. Rev. Fluid Mech.*, *40*, 71–90, doi:10.1146/annurev.fluid.40.111406.102208.

Gisler, G. R., R. P. Weaver, C. L. Mader, and M. L. Gittings (2003), Two- and three-dimensional simulations of asteroid ocean impacts, *Sci. Tsunami Hazards*, *21*, 119–130.

Gisler, G. R., R. P. Weaver, C. L. Mader, and M. L. Gittings (2004), Two- and three-dimensional asteroid impact simulations, *Comput. Sci. Eng.*, *6*, 46–55, doi:10.1109/MCISE.2004.1289308.

Gittings, M. L. (1992), SAIC's Adaptive grid Eulerian Hydrocode, paper presented at Numerical Methods Symposium, Def. Nucl. Agency, 28–30 Apr.

Glasstone, S., and P. J. Dolan (1977), *The Effects of Nuclear Weapons*, 653 pp., U.S. Gov. Print. Off., Washington, D. C.

Glimsdal, S., G. K. Pedersen, H. P. Langtangen, V. Shuvalov, and H. Dypvik (2007), Tsunami generation and propagation from the Mjølnir asteroid impact, *Meteorit. Planet. Sci.*, *42*, 1473–1493, doi:10.1111/j.1945-5100.2007.tb00586.x.

Hills, J. G., and M. P. Goda (1993), The fragmentation of small asteroids in the atmosphere, *Astron. J.*, *105*(3), 1114–1144, doi:10.1086/116499.

Hills, J. G., I. V. Nemchinov, S. P. Popov, and A. V. Teterev (1994), Tsunami generation by small asteroid impacts, in *Hazards From Comets and Asteroids*, edited by T. Gehrels, pp. 779–789, Univ. of Ariz. Press, Tucson.

Holsapple, K. A. (1993), The scaling of impact processes in planetary sciences, *Annu. Rev. Earth Planet. Sci.*, *21*, 333–373, doi:10.1146/annurev.ea.21.050193.002001.

Holsapple, K. A., and K. R. Housen (2007), A crater and its ejecta: An interpretation of Deep Impact, *Icarus*, *187*, 345–356, doi:10.1016/j.icarus.2006.08.029.

Holsapple, K. A., and R. M. Schmidt (1987), Point source solutions and coupling parameters in cratering mechanics, *J. Geophys. Res.*, *92*, 6350–6376, doi:10.1029/JB092iB07p06350.

Housen, K. R., and K. A. Holsapple (2003), Impact cratering on porous asteroids, *Icarus*, *163*, 102–119, doi:10.1016/S0019-1035(03)00024-1.

Ivanov, B. A. (2007), Size-frequency distribution of asteroids and impact craters: Estimates of impact rate, in *Catastrophic Events Caused by Cosmic Objects*, edited by V. V. Adushkin and I. V. Nemchinov, pp. 91–116, doi:10.1007/978-1-4020-6452-4_2, Springer, Dordrecht, Netherlands.

Ivanov, B. A., D. Deniem, and G. Neukum (1997), Implementation of dynamic strength models into 2D hydrocodes: Applications for atmospheric breakup and impact cratering, *Int. J. Impact Eng.*, *20*, 411–430, doi:10.1016/S0734-743X(97)87511-2.

Kenkmann, T., G. S. Collins, A. Wittmann, K. Wünnemann, W. U. Reimold, and H. J. Melosh (2009), A model for the formation of the Chesapeake Bay impact crater as revealed by drilling and numerical simulations, *Spec. Pap. Geol. Soc. Am.*, *458*, 571–585.

Korycansky, D. G., and P. J. Lynett (2005), Offshore breaking of impact tsunami: The Van Dorn effect revisited, *Geophys. Res. Lett.*, *32*, L10608, doi:10.1029/2004GL021918.

Korycansky, D. G., and P. Lynett (2007), Runup from impact tsunami, *Geophys. J. Int.*, *170*, 1076–1088, doi:10.1111/j.1365-246X.2007.03531.x.

Kyte, F. T., et al. (1981), High noble-metal concentrations in a Late Pliocene sediment, *Nature*, *292*, 417–420, doi:10.1038/292417a0.

Landau, L. D., and E. M. Lifshitz (1959), *Fluid Mechanics*, Pergamon, New York.

Lindström, M., E. F. F. Sturkell, J. Ormö, and R. Törnberg (1996), The Lockne marine impact in the Ordovician of central Sweden, *Meteorit. Planet. Sci.*, *31*, A80.

Lindström, M., V. Shuvalov, and B. Ivanov (2005), Lockne crater as a result of marine-target oblique impact, *Planet. Space Sci.*, *53*, 803–815, doi:10.1016/j.pss.2005.02.005.

Lynett, P., and P. L.-F. Liu (2005), A numerical study of the run-up generated by three-dimensional landslides, *J. Geophys. Res.*, *110*, C03006, doi:10.1029/2004JC002443.

Lynett, P., T.-R. Wu, and P. L.-F. Liu (2002), Modeling wave run-up with depth-integrated equations, *Coastal Eng.*, *46*(2), 89–107, doi:10.1016/S0378-3839(02)00043-1.

Lynett, P., J. Borrero, P. L.-F. Liu, and C. E. Synolakis (2003), Field survey and numerical simulations: A review of the 1998 Papua New Guinea tsunami, *Pure Appl. Geophys.*, *160*, 2119–2146, doi:10.1007/s00024-003-2422-0.

Lyon, S. P., and J. D. Johnson (1992), SESAME: The LANL equation of state database, *Rep. LA-UR-92-3407*, Los Alamos Natl. Lab., Los Alamos, N. M.

Mader, C. L. (1988), *Numerical Modeling of Water*, Univ. of Calif. Press, Berkeley.

McGlaun, J. M., and S. L. Thompson (1990), CTH: A three-dimensional shock wave physics code, *Int. J. Impact Eng.*, *10*, 351–360, doi:10.1016/0734-743X(90)90071-3.

McKinnon, W. B. (1982), Impact into the Earth's ocean floor: Preliminary experiments, a planetary model, and possibilities for detection, in *Geological Implications of Impacts of Large Asteroids and Comets on the Earth*, edited by L. T. Silver and P. H. Schultz, *Spec. Pap. Geol. Soc. Am.*, *190*, 129–142.

Melosh, H. J. (1982), The mechanics of large meteoroid impacts in the Earth's ocean, in *Geological Implications of Impacts of Large Asteroids and Comets on the Earth*, edited by L. T. Silver and P. H. Schultz, *Spec. Pap. Geol. Soc. Am.*, *190*, 121–127.

Melosh, H. J. (1989), *Impact Cratering: A Geological Process*, 245 pp., Oxford Univ. Press, New York.

Melosh, H. J. (2003), Impact-generated tsunamis: An overrated hazard, *Proc. Lunar Planet. Sci. Conf.* [CD-ROM], *34*, 2013.

Milner, D. J. (2007), Simulations of oceanic impact events, Ph.D. thesis, 236 pp., Univ. of Kent, Canterbury, U. K.

Milner, D. J., E. C. Baldwin, and M. J. Burchell (2007), Influence of a water layer on the impact cratering process and the fate of the projectile, paper presented at Bridging the Gap II: Effect of Target Properties on the Impact Cratering Process, Lunar and Planet. Inst., Saint-Hubert, Que., Canada, 22–26 Sept.

Near-Earth Object Science Definition Team (2003), Study to determine the feasibility of extending the search for near-Earth objects to smaller limiting diameters, report, 166 pp., Greenbelt, Md.

Neukum, G., B. A. Ivanov, and W. K. Hartmann (2001), Cratering records in the inner solar system in relation to the lunar reference system, *Space Sci. Rev.*, *96*, 55–86. (Reprinted in *Chronology and Evolution of Mars*, edited by R. Kallenbach et al., Kluwer, Dordrecht, Netherlands, 2001.)

Okal, E. A., and C. E. Synolakis (2004), Source discriminants for near-field tsunamis, *Geophys. J. Int.*, *158*, 899–912, doi:10.1111/j.1365-246X.2004.02347.x.

O'Keefe, J. D., and T. J. Ahrens (1982), The interaction of the Cretaceous/Tertiary extinction bolide with the atmosphere, ocean and solid Earth, in *Geological Implications of Impacts of Large Asteroid and Comets on the Earth*, edited by L. T. Silver and P. H. Schultz, *Spec. Pap. Geol. Soc. Am.*, *190*, 103–109.

O'Keefe, J. D., and T. J. Ahrens (1999), Complex craters: Relationship of stratigraphy and rings to impact conditions, *J. Geophys. Res.*, *104*(E11), 27,091–27,104, doi:10.1029/1998JE000596.

Olevson, K. L. R. (1969), Energy balance for transient water craters, *U.S. Geol. Surv. Prof. Pap.*, *650-D*, D189–D194.

Ormö, J., and M. Lindström (2000), When a cosmic impact strikes the sea bed, *Geol. Mag.*, *137*, 67–80, doi:10.1017/S0016756800003538.

Ormö, J., and H. Miyamoto (2002), Computer modeling of the water resurge at a marine impact: The Lockne crater, Sweden, *Deep Sea Res., Part II*, *49*, 983–994, doi:10.1016/S0967-0645(01)00143-6.

Ormö, J., V. V. Shuvalov, and M. Lindström (2002), Numerical modeling for target water depth estimation of marine-target impact craters, *J. Geophys. Res.*, *107*(E12), 5120, doi:10.1029/2002JE001865.

Peregrine, D. H. (1967), Long waves on a beach, *J. Fluid Mech.*, *27*(4), 815–827, doi:10.1017/S0022112067002605.

Pierazzo, E., and G. S. Collins (2004), A brief introduction to hydrocode modelling of impact cratering, in *Impact Studies: Cratering in Marine Environments and on Ice*, edited by H. Dypvik, M. Burchell, and P. Claeys, pp. 323–341, Springer, New York.

Pierazzo, E., et al. (2008), Validation of numerical codes for impact and explosion cratering: Impacts on strengthless and metal targets, *Meteorit. Planet. Sci.*, *43*(12), 1917–1938, doi:10.1111/j.1945-5100.2008.tb00653.x.

Schmidt, R. M. (1980), Meteor crater: Energy of formation—Implications of centrifuge scaling, *Proc. Lunar Planet. Sci. Conf., 11th*, 2099–2128.

Schmidt, R. M., and K. R. Housen (1987), Some recent advantages in the scaling of impact and explosion cratering, *Int. J. Impact Eng.*, *5*, 543–560, doi:10.1016/0734-743X(87)90069-8.

Shuvalov, V. V. (1999), Multi-dimensional hydrodynamic code SOVA for interfacial flows: Application to the thermal layer effect, *Shock Waves*, *9*, 381–390, doi:10.1007/s001930050168.

Shuvalov, V. V. (2002), Numerical modeling of impacts into shallow sea, in *Impacts in Precambrian Shields*, edited by J. Plado and L. J. Pesonen, pp. 323–336, Springer, New York.

Shuvalov, V. V., and I. A. Trubetskaya (2002), Numerical modeling of marine impacts, *Sol. Syst. Res.*, *36*, 417–430, doi:10.1023/A:1020467522340.

Shuvalov, V., H. Dypvik, and F. Tsikalas (2002), Numerical simulations of the Mjølnir marine impact crater, *J. Geophys. Res.*, *107*(E7), 5047, doi:10.1029/2001JE001698.

Shuvalov, V., J. Ormö, and M. Lindström (2005), Hydrocode simulations of the Lockne marine target impact event, in *Impact Tectonics*, edited by C. Koeberl and H. Henkel, pp. 405–422, doi:10.1007/3-540-27548-7_16, Springer, Berlin.

Stöffler, D. (1972), Deformation and transformation of rock-forming minerals by natural and experimental shock processes: I. Behavior of minerals under shock compression, *Fortschr. Mineral.*, *49*, 50–113.

Synolakis, C. E., and L. Kong (2006), Runup measurements of the December 26, 2004 tsunami, *Earthquake Spectra*, *22*(S3), S67–S91, doi:10.1193/1.2218371.

Thompson, S. L., and H. S. Lauson (1972), *Improvements in the Chart D Radiation-Hydrodynamic Code 3: Revised Analytic Equation of State*, 119 pp., Sandia Lab., Albuquerque, N. M.

Tillotson, J. M. (1962), *Metallic Equation of State for Hypervelocity Impact*, 141 pp., Adv. Res. Proj. Agency, San Diego, Calif.

Titov, V. V., A. B. Rabinovich, H. O. Mofjeld, R. E. Thomson, and F. I. Gonzalez (2005), The global reach of the 26 December 2004 Sumatra tsunami, *Science*, *309*, 2045–2048, doi:10.1126/science.1114576.

Toon, O. B., K. Zahnle, D. Morrison, R. P. Turco, and C. Covey (1997), Environmental perturbations caused by the impacts of asteroids and comets, *Ann. N. Y. Acad. Sci.*, *822*, 401–402.

van Dorn, W. G., and B. Le Mehaute (1968), Handbook of explosion-generated, water waves, *Rep. TC-130*, 192 pp., Tetra Tech, Pasadena, Calif.

von Dalwigk, I., and J. Ormö (2001), Formation of resurge gullies at impacts at sea: The Lockne crater, Sweden, *Meteorit. Planet. Sci.*, *36*, 359–369, doi:10.1111/j.1945-5100.2001.tb01879.x.

Ward, S. N. (2002), Planetary cratering: A probabilistic approach, *J. Geophys. Res.*, *107*(E4), 5023, doi:10.1029/2000JE001343.

Ward, S. N., and E. Asphaug (2000), Asteroid impact tsunami: A probabilistic hazard assessment, *Icarus*, *145*, 64–78, doi:10.1006/icar.1999.6336.

Ward, S. N., and E. Asphaug (2003), Asteroid impact tsunami of 2880 March 16, *Geophys. J. Int.*, *153*, F6–F10, doi:10.1046/j.1365-246X.2003.01944.x.

Weiss, R., and K. Wünnemann (2007), Large waves caused by oceanic impacts of meteorites, in *Tsunami and Nonlinear Waves*, edited by A. Kunda, pp. 235–260, Springer, New York.

Weiss, R., K. Wünnemann, and H. Bahlburg (2006), Numerical modelling of generation, propagation and run-up of tsunamis caused by oceanic impacts: Model strategy and technical solutions, *Geophys. J. Int.*, *167*, 77–88, doi:10.1111/j.1365-246X.2006.02889.x.

Worthington, A. M. (1908), *A Study of Splashes*, Longmans, Green, London.

Worthington, A. M., and R. S. Cole (1897), Impact with a liquid surface, studied by the aid of instantaneous photography, *Philos. Trans. R. Soc. London, Ser. A*, *189*, 137–148.

Wünnemann, K., and B. A. Ivanov (2003), Numerical modelling of the impact crater depth-diameter dependence in an acoustically fluidized target, *Planet. Space Sci.*, *51*, 831–845, doi:10.1016/j.pss.2003.08.001.

Wünnemann, K., and M. A. Lange (2002), Numerical modeling of impact-induced modifications of the deep-sea floor, *Deep Sea Res., Part II*, *49*, 969–981, doi:10.1016/S0967-0645(01)00148-5.

Wünnemann, K., G. S. Collins, and H. J. Melosh (2006), A strain-based porosity model for use in hydrocode simulations of impacts and implications for transient crater growth in porous targets, *Icarus*, *180*, 514–527, doi:10.1016/j.icarus.2005.10.013.

Wünnemann, K., R. Weiss, and K. Hofmann (2007), Characteristics of oceanic impact-induced large water waves—Re-evaluation of the tsunami hazard, *Meteorit. Planet. Sci.*, *42*, 1893–1903, doi:10.1111/j.1945-5100.2007.tb00548.x.

G. S. Collins, Impacts and Astromaterials Research Centre, Department of Earth Science and Engineering, Imperial College London, London SW7 2AZ, UK. (g.collins@imperial.ac.uk)

R. Weiss, Department of Geology and Geophysics, Texas A&M University, College Station, TX 77843, USA. (weiszr@tamu.edu)

K. Wünnemann, Museum für Naturkunde, Leibniz Institute at the Humboldt-Universität zu Berlin, Invalidenstraße 43, D-10115 Berlin, Germany. (kai.wuennemann@mfn-berlin.de)